Research Square

Preprints are preliminary reports that have not undergone peer review.
They should not be considered conclusive, used to inform clinical practice,
or referenced by the media as validated information.

Myometrial contraction-activated endometrial PIEZO2 safeguards fertility under maternal stress

Ren-Wei Su

renweisu@scau.edu.cn

South China Agricultural University https://orcid.org/0000-0002-5290-6651

Jin-Wen Kang

South China Agricultural University https://orcid.org/0000-0003-2620-9286

Yu Zhang

South China Agricultural University

Hui-Xia Li

South China Agricultural University

He Zou

South China Agricultural University

Jing-Yi Yang

South China Agricultural University

Xiao-Qing Huang

South China Agricultural University

Jia-Ying Yu

South China Agricultural University

Zi-Wei Ai

Hubei University of Medicine

Ying Zhang

Hubei University of Medicine

Rui Zhang

South China Agricultural University

Ying-Nan Liu

South China Agricultural University

Zeng-Ming Yang

Guizhou University https://orcid.org/0000-0001-6016-5710

Bin Guo

Jilin University https://orcid.org/0000-0001-5950-8974

Hong-Lu Diao

Hubei University of Medicine

Article

Keywords:

Posted Date: October 27th, 2026

DOI: https://doi.org/10.21203/rs.3.rs-11028741/v1

License: This work is licensed under a Creative Commons Attribution 4.0 International License.
Read Full License

Additional Declarations: There is **NO** Competing Interest.

Myometrial contraction-activated endometrial PIEZO2 safeguards fertility under maternal stress

Jin-Wen Kang[1]†, Yu Zhang[1]†, Hui-Xia Li[1], He Zou[1], Jing-Yi Yang[1], Xiao-Qing Huang[1], Jia-Ying Yu[1], Zi-Wei Ai[2], Ying Zhang[2], Rui Zhang[1], Ying-Nan Liu[1], Zeng-Ming Yang[3]*, Bin Guo[4]*, Hong-Lu Diao[2]*, Ren-Wei Su[1]*

Affiliations:

[1]College of Veterinary Medicine, South China Agricultural University, Guangzhou, China

[2]Reproductive Medicine Center of Renmin Hospital, Biomedical Engineering College, Hubei University of Medicine, Shiyan, Hubei, China

[3]College of Animal Science, Guizhou University, Guiyang, China

[4]College of Veterinary Medicine, Jilin University, Changchun, China

†These authors contributed equally to this work

***Correspondence**

Ren-Wei Su, PhD.

483 Wushan Road, Guangzhou, Guangdong, China, 510642

Email: renweisu@scau.edu.cn

Hong-Lu Diao, PhD.

39 Chaoyang Middle Road, Shiyan, Hubei, China, 442000

Email: hldiao@hbmu.edu.cn

Bin Guo, PhD.

5333 Xi`an Road, Changchun, Jilin, China, 130062

Email: guobin79@jlu.edu.cn

Zeng-Ming Yang, PhD.

2708 Huaxi District, Guiyang, Guizhou, China, 550025

Email: yangzm@gzu.edu.cn

Abstract

Embryo implantation requires a receptive uterine environment that integrates hormonal and mechanical cues. The uterus contracts throughout the reproductive cycle, and maternal stress increases uterine contractility and impairs implantation, yet how the endometrium senses and adapts to these mechanical disturbances has remained unknown. Here we show that the mechanosensitive ion channel PIEZO2 in the endometrium converts myometrial contraction into progesterone receptor (PGR) transcription, thereby safeguarding implantation under maternal stress. Using endometrium-specific *Piezo2* knockout mice, we find that PIEZO2 is dispensable for implantation under basal conditions but becomes essential when stress elevates uterine contractility, with its loss causing implantation failure. Mechanistically, hypercontraction activates PIEZO2 to drive collagen deposition and focal adhesion kinase (FAK)–Hippo/YAP–TEAD signaling, which directly reinforces PGR transcription. This cascade is conserved in human endometrium and is diminished in patients with recurrent implantation failure. Our findings show that the endocrine control of implantation is itself mechanically gated, defining a mechanism through which maternal stress compromises fertility and identifying PIEZO2 as a potential therapeutic entry point.

Main

Infertility affects 8–12% of couples worldwide, with an estimated 30% of embryos lost prior to successful implantation[1,2]. Successful implantation demands a receptive endometrium and the precise orchestration of ovarian steroid hormones, particularly progesterone, and dynamic structural remodeling of uterine tissue. During the peri-implantation window, progesterone acts through its nuclear receptor, PGR, to drive the differentiation of endometrial stromal cells (ESCs) into decidual cells. This transformation is essential for endometrial receptivity, and subsequent trophoblast invasion and placental development[2-4]. The progesterone receptor exists as two principal isoforms, PGR-A and PGR-B, which exert distinct and sometimes opposing functions in the endometrium, with PGR-A being a primary driver of progesterone-dependent endometrial transformation[5]. Impaired progesterone responsiveness, commonly referred to as 'progesterone resistance,' is strongly associated with implantation failure and is increasingly recognized as a central feature of endometrial disorders, including endometriosis-related infertility and recurrent implantation failure (RIF)[6,7]. Despite PGR transcriptional and post-translational regulation being extensively examined, the upstream signals that modulate PGR expression during the dynamic peri-implantation period remain incompletely characterized.

Uterine contractions represent a prominent mechanical activity throughout the reproductive cycle, with accumulating evidence suggesting that mechanical forces in the uterus function as underappreciated determinants of implantation success[8]. Physiological myometrial peristalsis facilitates sperm transport, embryo positioning within the uterine cavity, and menstrual discharge[8-12]. However, it is increasingly recognized that excessive or dysregulated contractility during the implantation window is detrimental to pregnancy establishment[13-17]. Clinical studies using transvaginal ultrasonography and uterine electromyography have demonstrated that elevated uterine peristalsis correlates with reduced implantation rates in assisted reproductive technologies, and that pharmacological suppression of uterine contractions at the time of embryo transfer can improve pregnancy outcomes in select patient populations[18,19]. Aberrant uterine contractions are further linked to conditions such as RIF and endometriosis-related infertility, where hyperperistalsis may physically dislodge embryos or disrupt the endometrial signaling environment[20,21]. Critically, maternal psychological stress increases uterine contractility through activation of the hypothalamic-pituitary-adrenal (HPA) axis and sympathetic nervous system[22-28], raising the possibility that stress-induced mechanical disturbances actively challenge the establishment of uterine receptivity. Despite these clinical observations, a fundamental question remains unanswered: can the

endometrium sense and adapt to the abnormal mechanical forces generated by uterine hypercontraction?

Mechanosensitive ion channels provide a fundamental mechanism by which cells detect and respond to physical forces[29]. The PIEZO family, comprising PIEZO1 and PIEZO2, are evolutionarily conserved mechanotransducers that form large trimeric complexes in the plasma membrane and convert membrane tension directly into an intracellular Ca^{2+} influx. PIEZO1 has been implicated in vascular development, bone homeostasis, immune cell mechanosensing, and intestinal stem cell fate determination, whereas PIEZO2 is best characterized as the principal mechanotransducer for light touch and proprioception in sensory neurons[30-41]. While PIEZO channels in the myometrium are known to contribute to parturition-associated uterine contractions[38,42,43], their specific function within the endometrium to detect mechanical perturbations during early pregnancy remains poorly characterized. In particular, it remains unclear whether ESCs possess a mechanosensing apparatus capable of translating contraction-derived mechanical stress into adaptive molecular responses to safeguard implantation.

Herein, PIEZO2 was identified as a key mechanosensor in ESCs that is dispensable for implantation under physiological conditions but becomes essential when maternal stress elevates uterine contractility. Utilizing an endometrium-specific *Piezo2* conditional knockout (*Piezo2*$^{d/d}$) mouse model, stress-induced hypercontraction was shown to activate PIEZO2-dependent Ca^{2+} signaling and promote collagen (COL) deposition through IGF1-mediated paracrine communication among stromal subpopulations. The PIEZO2-COL mechanotransduction cascade then cooperatively activates focal adhesion kinase (FAK)-Hippo signaling, drives Yes-associated protein (YAP) nuclear translocation, and directly enhances *Pgr* transcription through TEA domain (TEAD) transcription factors-responsive elements—thereby reinforcing progesterone responsiveness under conditions of maternal stress. We further demonstrated that this signaling axis is conserved in human ESCs and is diminished in patients with RIF. These findings establish a mechanosensing paradigm in which myometrial contraction activates PIEZO2, converting mechanical stress into a reinforcement of hormonal responses and revealing that endocrine regulation of implantation is itself mechanically gated.

PIEZO2 safeguards embryo implantation under maternal stress

PIEZO2 expression was examined in the mouse uterus. *Piezo2* mRNA was predominantly expressed in endometrial stromal cells and markedly upregulated during the peri-implantation period (**Fig. 1, A and B**), although uterine *Piezo2* levels were extremely lower than those in dorsal root ganglion (DRG) (**Extended data Fig. 1A**). To investigate its physiological function, endometrium-specific *Piezo2* conditional knockout mice were generated by crossing floxed *Piezo2* (*Piezo2*$^{f/f}$) with *Pgr-Cre* (*Pgr*$^{Cre/+}$) transgenic mice, producing *Pgr*$^{Cre/+}$*Piezo2*$^{f/f}$ (*Piezo2*$^{d/d}$) females and *Piezo2*$^{f/f}$ littermates as controls (**Extended data Fig. 1, B to E**). Fertility testing showed that *Piezo2*$^{d/d}$ females produced significantly lower litter size (5.95 ± 0.125 vs. 7.80 ± 0.122 pups/litter) and lighter pups (1.16 ± 0.005 vs. 1.37 ± 0.002 g) compared to *Piezo2*$^{f/f}$ controls (**Extended data Table 1**), indicating impaired reproductive performance.

To localize the defect, embryo implantation was assessed at 4.5 days post coitum (dpc) across four independent breeding trials. While all control mice displayed implantation sites, *Piezo2*$^{d/d}$ females showed highly variable implantation rates (0% to 80%) (**Fig. 1C**), an incomplete and inconsistent penetrance indicative of a fluctuating extrinsic factor rather than a fully penetrant intrinsic defect. As ambient noise from daily animal facility activities represents a highly variable environmental factor, implantation was tested under controlled acoustic conditions. *Piezo2*$^{f/f}$ mice implanted consistently in both quiet (45 ± 5 dB) and noisy (65 ± 5 dB) environments, whereas *Piezo2*$^{d/d}$ mice showed consistent implantation under quiet conditions but complete implantation failure under noisy conditions (**Extended data Fig. 1, F and G**). Thus, ambient environmental stress is sufficient to precipitate implantation failure in the absence of PIEZO2, prompting the adoption of a standardized stress model for subsequent experiments.

Given that environmental and psychological stress negatively affect pregnancy outcomes[44-46], a modified Single Prolonged Stress (SPS)-based protocol[47,48] consisting of daily multimodal stress exposure was implemented in *Piezo2*$^{d/d}$ and *Piezo2*$^{f/f}$ mice from 0.5 to 3.5 dpc under controlled quiet acoustic conditions to exclude confounding auditory stress (**Extended data Fig. 1H**). SPS markedly increased serum corticosterone levels in both genotypes, confirming successful stress induction (**Extended data Fig. 1I**). Without stress exposure, both groups displayed comparable implantation numbers. However, SPS treatment completely abolished implantation in *Piezo2*$^{d/d}$ (SPS-*Piezo2*$^{d/d}$) mice while leaving SPS-*Piezo2*$^{f/f}$ unaffected (**Fig. 1, D and E**). In striking contrast to *Piezo2*$^{f/f}$ controls, which maintained normal implantation until challenged with a much stronger stressor (3 h restraint plus 20 min swimming), all *Piezo2*$^{d/d}$ mice failed to implant following only light stress exposure (0.5 h restraint plus 3 min swimming),

revealing a profound susceptibility of *Piezo2*$^{d/d}$ females to stress-induced implantation failure (**Extended data Fig. 1J**). Morphologically normal blastocysts were recovered from the uterine lumen of SPS-*Piezo2*$^{d/d}$ mice (**Fig. 1D**), and blastocyst number together with serum estradiol (E2) and progesterone (P4) were comparable to SPS-*Piezo2*$^{f/f}$ (**Extended data Fig. 2, A to C**), excluding impaired ovarian function or defective preimplantation development. Histological analysis further revealed that the blastocysts remained unattached in SPS-*Piezo2*$^{d/d}$ uteri, and the implantation site was devoid of COX2 expression, suggesting defective endometrial receptivity (**Fig. 1, F and G**). A reciprocal embryo transfer experiment showed that embryos collected from SPS-*Piezo2*$^{d/d}$ mice successfully implanted when transferred into SPS-*Piezo2*$^{f/f}$ uteri, whereas embryos from SPS-*Piezo2*$^{f/f}$ completely failed to implant in SPS-*Piezo2*$^{d/d}$ uteri (**Fig. 1, H and I**). These results unequivocally demonstrate that stress-induced implantation failure in *Piezo2*$^{d/d}$ mice is attributable to defective endometrial receptivity rather than embryonic abnormalities, PIEZO2 is dispensable under basal conditions but becomes essential for maintaining uterine receptivity under stress.

PIEZO1 and PIEZO2 are closely related mechanosensitive ion channels co-expressed in the uterine endometrium[49]. To determine whether the stress-protective function was specific to PIEZO2, we examined the response of both channels to SPS. SPS selectively upregulated *Piezo2* but not *Piezo1* (**Extended data Fig. 2, D and E**), and implantation in *Piezo1*$^{d/d}$ mice remained stable and unaffected under SPS (**Extended data Fig. 2F**), indicating a non-redundant and specific role for PIEZO2 in stress-dependent implantation protection. Primers targeting *Piezo2* exons 17 to 18, upstream of the floxed region (exons 22 to 24), further revealed that SPS increased *Piezo2* transcription only when functional PIEZO2 protein was present, indicating positive autoregulatory feedback in which channel activity amplifies its own expression (**Extended data Fig. 2E**).

PIEZO2 preserves uterine receptivity by increasing progesterone responsiveness under maternal stress

Having established that PIEZO2 is required for endometrial receptivity during maternal stress, hormonal axis downstream was examined, as receptivity is governed by ovarian steroids[50]. Circulating E2 and P4 were unchanged, yet SPS significantly increased endometrial ESR1 (ERα) expression in both genotypes (**Fig. 2A**), whereas PGR was strongly induced by SPS in *Piezo2*$^{f/f}$ but failed to increase in *Piezo2*$^{d/d}$ mice (**Fig. 2B**). Consistent with this imbalance, estrogen-responsive genes (*Muc1*, *Muc4*, *Ltf*)[50] were markedly elevated in SPS-*Piezo2*$^{d/d}$ uteri (**Fig. 2, C and D**), whereas progesterone-responsive genes (*Hoxa10*,

Hand2, *Areg*)[50] were significantly reduced relative to SPS-treated controls (**Fig. 2, D and E**), shifting the endometrium toward estrogen dominance. Progesterone-driven stromal cell proliferation[51] was likewise reduced in SPS-*Piezo2*$^{d/d}$ uteri, as assessed by Ki67 immunohistochemistry (**Fig. 2D**).

To determine whether defective progesterone signaling is the proximate cause of implantation failure, SPS-*Piezo2*$^{d/d}$ mice were supplemented with exogenous progesterone (**Extended data Fig. 3A**). Progesterone fully restored implantation in all tested SPS-*Piezo2*$^{d/d}$ mice (100%, n = 10), with implantation site number, morphology and weight comparable to SPS-treated controls (**Fig. 2, F to H, Extended data Fig. 3B**). Correspondingly, progesterone supplementation reversed estrogen dominance in both directions: elevated estrogen-responsive genes returned to control levels while suppressed progesterone-responsive genes were restored (**Extended data Fig. 3C**). Furthermore, progesterone restored COX2 expression, indicating restored receptivity (**Fig. 2H)**. Implantation failure in SPS-*Piezo2*$^{d/d}$ uteri therefore stems directly from a hormone-response imbalance caused by impaired PGR signaling, placing PGR downstream of PIEZO2.

Uterine contraction-derived mechanical forces activate endometrial PIEZO2

While PIEZO2 is required for stress-induced implantation-protection and PGR upregulation, how stress activates PIEZO2 remained unclear. Because maternal stress increases uterine contractility via neuroendocrine pathways, we hypothesized that contraction-generated mechanical forces serve as the physiological trigger for PIEZO2 activation in mouse endometrial stromal cells. Although SPS significantly increased the frequency and amplitude of uterine peristalsis in both genotypes, SPS-*Piezo2*$^{d/d}$ uteri exhibited attenuated contractions comparable to those of NON-SPS-*Piezo2*$^{f/f}$ uteri (**Fig. 3, A and B**). The uterus comprises two functionally distinct compartments, the myometrium, which governs contractility, and the endometrium, which supports embryo implantation and development. *Piezo2* deletion was specifically in the endometrium but not myometrium (**Fig. 3C**). Given that nitric oxide (NO) signaling suppresses uterine contractility[52], nitric oxide synthase (NOS) isoforms were examined, and found to be elevated in *Piezo2*$^{d/d}$ endometrium (**Extended data Fig. 4, A and B**). Pharmacological inhibition of NOS with L-NAME HCl restored uterine contractility, but induced implantation failure in *Piezo2*$^{d/d}$ mice even without SPS (**Extended data Fig. 4, B to G**). in the absence of PIEZO2, endometrial cells thus produce excess NO that diffuses to the myometrium and reduces contractility, masking the phenotype under basal conditions. Enhanced uterine contractions that accompany stress, while potentially disruptive to endometrial receptivity, serve as a key upstream trigger for PIEZO2 activation to protect

implantation via PGR upregulation.

To investigate whether mechanical stimulation activates PIEZO2 directly, isolated uteri were treated *ex vivo* with PGF2α, a potent inducer of myometrial contraction[53]. PGF2α increased contraction frequency and amplitude in both genotypes, though to a lesser extent in *Piezo2*$^{d/d}$ uteri (**Fig. 3, D and E**). PGF2α-induced contractions upregulated both *Piezo2* and *Pgr* expression in *Piezo2*$^{f/f}$ but not *Piezo2*$^{d/d}$ uteri (**Fig. 3F**), establishing a direct link between contraction-derived mechanical force and PIEZO2-dependent gene activation without systemic neuroendocrine input. To determine whether PGF2α mimics SPS treatment *in vivo*, PGF2α was administered from 0.5 to 3.5 dpc. PGF2α selectively reproduced the SPS phenotype in *Piezo2*$^{d/d}$ mice, causing implantation failure and an amplified estrogen response without PGR and its target genes induction (**Fig. 3, G to I**). Applying mechanical stretch directly to isolated uteri elicited rapid *Piezo2* and *Pgr* transcription in *Piezo2*$^{f/f}$ uteri, a response completely absents in *Piezo2*$^{d/d}$ uteri (**Fig. 3J**), demonstrating that force alone, without any pharmacological or hormonal intermediate, is sufficient. Together, these results demonstrate that uterine mechanical forces generated by myometrial contractions activate PIEZO2-mediated mechanotransduction to promote PGR expression in endometrial stromal cells and protect implantation.

PIEZO2 remodels the endometrial extracellular matrix to support progesterone signaling

PIEZO2 is gated directly by mechanical force and lacks known endogenous chemical ligands, so its loss is expected to manifest as a transcriptional state change in mechanical loaded cells. To identify PIEZO2-dependent transcriptional programs promoting PGR expression, single-cell RNA sequencing (scRNA-seq) was performed on uteri from SPS-treated mice at 3.5 dpc. A total of 18,877 cells (SPS-*Piezo2*$^{f/f}$, 10,678; SPS-*Piezo2*$^{d/d}$, 8,199) resolved into 14 clusters (**Extended data Fig. 5A**). Major uterine cell types were well separated expressing corresponding marker genes and overlapped extensively between genotypes in UMAP embedding (**Extended data Fig. 5, A and B**), indicating that *Piezo2* deletion does not alter cellular composition and that any difference must lie within a cell state rather than in cell identity. Fibroblasts represented the largest population but were significantly reduced in PIEZO2-deficient uteri (SPS-*Piezo2*$^{f/f}$, 62.94% vs. SPS-*Piezo2*$^{d/d}$, 55.56%) (**Extended data Fig. 5B**), consistent with reduced Ki67-positive stromal proliferation (**Fig. 2D**) and suggesting that PIEZO2 contributes to stromal maintenance during the peri-implantation window.

Because uterine mesenchyme comprises endometrial fibroblasts, myometrial smooth muscle cells, and

perivascular cells, a stepwise gating strategy based on established markers was applied before sub-clustering. Cells expressing *Acta2* or *Myh11* were excluded as smooth muscle[54,55]; *Vim*$^{-}$ cells were excluded as non-mesenchymal[56]; and cells positive for *Hoxa10*, a marker of endometrial stromal identity[57], and *Mmp2*, a marker of extracellular matrix (ECM) remodeling[58] were retained. Re-clustering this enriched population yielded six subclusters (**Fig. 4, A and B, Extended data Fig. 5C**). Subcluster 2 (S2) was markedly reduced in SPS-*Piezo2*$^{d/d}$ uteri compared with *Piezo2*$^{f/f}$ (SPS-*Piezo2*$^{f/f}$, 10.42% vs. SPS-*Piezo2*$^{d/d}$, 2.07%) (**Fig. 4, A and B**). Differentially expressed genes identified S2 as a matrix-producing stromal state, enriched in fibrillar collagens and matrix glycoproteins (**Fig. 4C**). Comparisons between genotypes revealed significantly reduced expression of multiple collagens and ECM-associated genes (*Col1a1*, *Col1a2*, *Col5a1*, *Col6a3*, *Col14a1*, *Gsn, Lum, Sparc*) in S2 from SPS-*Piezo2*$^{d/d}$ uteri (**Fig. 4D, Extended data Fig. 5D**). Masson's trichrome and type I collagen immunostaining confirmed that SPS increases collagen deposition in SPS-*Piezo2*$^{f/f}$ but not SPS-*Piezo2*$^{d/d}$ uteri (**Fig. 4, E and F**). Thus, PIEZO2-dependent signaling is required for maintenance of the matrix-producing stromal state and mechanical microenvironmental properties.

Piezo2 expression varied across fibroblast subclusters: high in S0, S1, S3, and S4, but minimal in S2 and S5 (**Extended data Fig. 5E**), indicating that loss of the matrix-producing state is non-cell-autonomous. Ligand-receptor interaction analysis rendered as a chord diagram showed that S0 and 1 had the highest connectivity, with a dominant Igf1-Igf1r axis directed to S2 and other subclusters (**Extended data Fig. 5, F and G**), suggesting PIEZO2-responsive cells sense mechanical stress and secrete IGF1 to drive ECM remodeling in neighboring cells. Consistent with this, *Igf1* mRNA was upregulated by SPS in SPS-*Piezo2*$^{f/f}$ but not SPS-*Piezo2*$^{d/d}$ uteri (**Extended data Fig. 5H**), and recombinant IGF1 restored collagen expression in *Piezo2*$^{d/d}$ primary mouse endometrial stromal cells (MESCs) (**Extended data Fig. 5I**), demonstrating that IGF1 acts downstream of the channel and bypasses PIEZO2 requirement for ECM production.

Having established that PIEZO2 promotes collagen deposition via IGF1 paracrine signaling, we examined whether ECM provides feedback to regulate PGR expression. *Piezo2*$^{f/f}$ MESCs cultured on increasing densities of collagen I (COL-I) upregulated *Piezo2* and *Pgr* in a density-dependent manner, whereas in *Piezo2*$^{d/d}$ MESCs collagen-induced *Pgr* upregulation was abolished (**Fig. 4, G and H**). Chelation of Ca^{2+} with BAPTA-AM blocked upregulation of *Pgr* in *Piezo2*$^{f/f}$ cells (**Fig. 4I**), indicating that PIEZO2-dependent Ca^{2+} signaling is required for collagen-mediated PGR induction. Notably, progesterone

supplementation rescued implantation (**Fig. 2, F to H)** without restoring collagen expression (**Fig. 4J**), placing ECM remodeling upstream of progesterone signaling.

PIEZO2-collagen cooperation activates the FAK-Hippo-YAP pathway to drive *Pgr* transcription

To determine how ECM remodeling regulates *Pgr*, downstream mechanotransduction was investigated. Collagen engages integrin to activate focal adhesion kinase (FAK)[59], while PIEZO1-derived Ca^{2+}/calmodulin-dependent protein kinase II (CaMKII) signaling can also promote FAK phosphorylation[60]. Given the requirement for PIEZO2-dependent Ca^{2+} in collagen-regulated *Pgr* expression, FAK was predicted to serve as a convergent signaling node at which the two mechanical inputs are integrated. As anticipated, *in vivo*, SPS increased FAK phosphorylation in *Piezo2*$^{f/f}$ but not *Piezo2*$^{d/d}$ uteri (**Fig. 5A, Extended data Fig. 6A**). In *Piezo2*$^{f/f}$ MESCs, phosphorylation of CaMKII and FAK, as well as *Pgr* mRNA upregulation was abolished by Ca^{2+} chelation (BAPTA-AM) or CaMKII inhibition (KN93) (**Fig. 5, B to D, Extended data Fig. 6, B and C**), showing that collagen alone is insufficient and requires PIEZO2-derived Ca^{2+}/CaMKII input. FAK inhibition with Y15 blocked collagen-induced *Pgr* expression (**Fig. 5, E and F, Extended data Fig. 6D**), confirming FAK as the convergence point uniting PIEZO2-Ca^{2+} and collagen-integrin signals.

FAK is an established upstream regulator of the Hippo-YAP pathway: it recruits and activates SRC family kinases, which inhibit the Hippo pathway kinases large tumor suppressor kinase 1/2 (LATS1/2), allowing dephosphorylated YAP/TAZ to enter the nucleus, bind TEAD transcription factors and drive target gene transcription[59]. Whether the PIEZO2-collagen-FAK axis converges on YAP/TAZ to regulate *Pgr* was therefore tested. In SPS-*Piezo2*$^{f/f}$ uteri, YAP phosphorylation decreased and nuclear YAP/TAZ accumulation increased whereas neither occurred in *Piezo2*$^{d/d}$ uteri (**Fig. 5, G and H, Extended data Fig. 6E**). TAZ was not resolved by western blot owing to its substantially lower uterine expression (**Extended data Fig. 6F**). In *Piezo2*$^{f/f}$ MESCs, collagen-induced YAP dephosphorylation was blocked by BAPTA-AM, KN93, or Y15 (**Fig. 5I, Extended data Fig. 6G**), placing YAP downstream of a Ca^{2+}/CaMKII→FAK→LATS1/2 relay. An 8×GTIIC luciferase reporter containing eight TEAD-responsive element (TRE)[61] confirmed that PIEZO2 and collagen cooperatively drive YAP-TEAD transcriptional activity (**Fig. 5J**). The relationship was then interrogated pharmacologically in both directions: LATS1/2 inhibition (TDI-011536, TDI) decreased phosphorylated YAP and restored *Pgr* expression in *Piezo2*$^{d/d}$ MESCs (**Fig. 5K, Extended data Fig. 6H**), whereas disruption of the YAP-TEAD interaction with verteporfin (VP) blocked collagen-induced *Pgr* expression (**Fig. 5L**).

Whether YAP-TEAD acts directly at the *Pgr* locus or through intermediates was resolved next. Bioinformatic analysis identified a putative TEAD-binding element in the proximal *Pgr* promoter[62], and luciferase assays with wild-type or mutant *Pgr* promoter constructs demonstrated that collagen activates the promoter in a PIEZO2-dependent manner, and response abolished by mutation of the TEAD binding site (**Fig. 5M, Extended data Fig. 6I**). This provides direct evidence that YAP-TEAD binds the *Pgr* promoter to drives transcription, establishing a mechanotranscriptional mechanism linking uterine mechanical forces and *Pgr* expression. Most importantly and informatively, administration of TDI *in vivo* to SPS-*Piezo2*$^{d/d}$ mice fully rescued implantation (**Fig. 5, N and O, Extended data Fig. 6J**), demonstrating that YAP reactivation bypass PIEZO2 deficiency and suggesting Hippo pathway targeting may represent a potential therapeutic strategy for stress-induced implantation failure.

The PIEZO2-PGR cascade is conserved in humans and is impaired in recurrent implantation failure

Since maternal stress and uterine hypercontractility have been linked to recurrent implantation failure (RIF)[63-66], to assess clinical relevance, endometrial biopsies from fertile controls and RIF patients (n = 8 per group; **Extended data Table 2**) were evaluated. Both PIEZO2 and PGR levels were significantly reduced in the endometrial stroma of RIF patients (**Fig. 6, A and B**) and showed strong positive correlation (**Fig. 6C**). Serum cortisol, a systemic marker of stress, was significantly elevated in RIF patients (**Extended data Fig. 7A**), linking maternal stress to impaired PIEZO2-PGR signaling in human endometrium.

Whether the mouse cascade operates node by node in human cells was then tested in human endometrial stromal cells (T-HESCs). COL-I coating upregulated *PIEZO2* and *PGR* expressions which were abolished in PIEZO2-knockdown (KD) cells (**Fig. 6D**). COL-I induced CaMKII and FAK phosphorylation in control but not PIEZO2-KD cells (**Fig. 6E, Extended data Fig. 7B**). Pharmacological inhibition of Ca^{2+} (BAPTA-AM), CaMKII (KN93), or FAK (Y15) blocked collagen-induced YAP dephosphorylation and *PGR* expression (**Fig. 6, E to G, Extended data Fig. 7, C and D**) LATS1/2 inhibition (TDI) rescued *PGR* expression in PIEZO2-KD cells, whereas YAP-TEAD inhibitor (verteporfin) suppressed *PGR* (**Fig. 6H**), confirming conservation of the entire PIEZO2-collagen-Ca^{2+}/CaMKII-FAK-Hippo-YAP-PGR cascade in human ESCs.

In RIF, PGR-mediated decidualization failure is considered a central determinant[3,4]. Therefore, i*n vitro* decidualization was assessed in T-HESCs. The decidualization markers *FOXO1*, *IGFBP1*, and *PRL* [67]

were significantly reduced in PIEZO2-KD cells (**Fig. 6I**). Overexpression of PGR-A, but not PGR-B, fully restored decidualization marker expression in PIEZO2-KD cells (**Fig. 6I, Extended data Fig. 7E**), identifying PGR-A as the principal downstream effector linking PIEZO2 mechanotransduction to decidualization and providing a mechanistic basis for RIF pathogenesis (**Fig. 6J**).

Collectively, these findings define a conserved mechanotransduction cascade linking uterine mechanical forces to progesterone responsiveness and endometrial receptivity. Diminished activity of this pathway in RIF patients implicates PIEZO2-dependent mechanosensing deficiency as a contributor to implantation failure in the clinic.

Discussion

The findings presented herein reveal a mechanosensing mechanism in the endometrium that converts uterine contraction-derived mechanical stress into PGR transcription, thereby providing resilience against stress-induced implantation failure. Specifically, myometrial contraction-activated mechanotransduction was found to upregulate PGR in ESCs, preventing implantation failure under maternal stress. Mechanistically, this process depends on PIEZO2, which senses the uterine mechanical microenvironment and ensures successful embryo implantation. These findings expand the functional role of PIEZO2 beyond neuronal sensory cells, highlighting its broader importance as a mechanotransducer in diverse cell types.

Embryo implantation requires a receptive endometrium that is precisely regulated by hormonal cues[3,7]. While progesterone signaling is essential for this process, how uterine receptivity is maintained under fluctuating environmental conditions remains largely unclear. Herein, PIEZO2 was identified as a mechanosensor that links uterine mechanical activity to progesterone responsiveness, thereby safeguarding implantation under maternal stress. A central finding of this study is that PIEZO2 is dispensable for implantation under basal conditions but becomes essential under maternal stress. This context-dependent requirement reveals that successful implantation depends not only on achieving receptivity, but also on sustaining it when challenged. Although maternal stress has been associated with adverse pregnancy outcomes, including RIF, conflicting clinical observations have left its role unresolved[63-66]. Our data suggest that stress-induced implantation failure depends on the disruption of a mechanosensing pathway, with endometrial PIEZO2 acting as a key buffering component.

Classically, uterine contractions have been associated with impaired implantation, but this study demonstrated that uterine contractions act as a physiological trigger for PIEZO2 activation. Elevated uterine contractility, commonly observed during ovarian stimulation in IVF and in pathological conditions such as endometriosis, has long been associated with impaired implantation[68-72]. Uterine hypercontractility is widely attributed to oxytocin and prostaglandin (PG)F2a by endometrial cells[73,74]. While this has made oxytocin receptor antagonists, such as atosiban, a logical pharmacological intervention, clinical outcomes remain variable[75,76]. Furthermore, conditions such as inflammation, endometriosis, adenomyosis, and reproductive physiological disorders can strengthen uterine contractions, leading to uterine hyperperistalsis, potentially causing dysmenorrhea and severe uterine cramps, thereby leading to implantation failure[77-79]. Our findings fundamentally reframe the paradigm on uterine contractions: rather than being merely a disruptive force, contraction-generated mechanical signals are sensed by PIEZO2 in

endometrial stromal cells, and when properly transduced, actively reinforce implantation competence. Notably, SPS acts a multimodal stressor whose systemic effects, including activating autonomic and HPA-axis neuroendocrine pathways, extends beyond uterine contractility. However, several lines of evidence support mechanical force as the critical mediator of PIEZO2-dependent implantation protection: (i) PGF2α-induced uterine contraction alone phenocopied the effect of SPS; (ii) direct mechanical stretching of isolated uteri was sufficient to induce *Piezo2* and *Pgr*; and (iii) even ambient noise levels encountered in standard animal facilities triggered implantation failure in *Piezo2*$^{d/d}$ mice. Together, these findings argue that while SPS activates multiple stress pathways, the mechanical component is both necessary and sufficient to induce the protective PIEZO2-dependent phenotype.

Mechanistically, a PIEZO2-collagen-FAK-Hippo-YAP signaling cascade that directly regulates *PGR* transcription was delineated. Specifically, PIEZO2-mediated Ca^{2+} influx cooperates with collagen-dependent focal adhesion signaling to activate FAK and suppress Hippo pathway activity, leading to YAP nuclear translocation. The Hippo-YAP pathway is a well-established mechanosensitive signaling axis that integrates extracellular mechanical cues with transcriptional responses[80,81]. This study demonstrated that YAP binds to a TEAD-responsive element within the *Pgr* promoter, directly driving its transcription. While previous studies have focused on post-translational regulation of PGR stability[82,83], this study revealed a mechanotranscriptional mechanism that modulates PGR expression. This redefines progesterone signaling as not solely a hormonally controlled process but also a mechanically regulated one: under maternal stress, PIEZO2-dependent mechanotransduction enhances PGR expression, maintaining progesterone responsiveness and preventing estrogen dominance, a condition frequently associated with implantation failure[84,85].

An unexpected finding of this study is the paracrine feedback circuit between the endometrium and myometrium: PIEZO2-deficient endometrial cells produce excess NO that suppresses myometrial contractility. This mechanism explains the attenuated contractility in *Piezo2*$^{d/d}$ uteri even in the absence of stress, and the masking of the implantation phenotype under basal conditions. Pharmacological removal of this NOS-mediated brake was sufficient to expose the PIEZO2-dependent implantation defect in the absence of external stress, demonstrating that the threshold of mechanical force—rather than stress per se—determines whether PIEZO2 engagement is required. This homeostatic buffering mechanism has implications for understanding why some women with elevated uterine contractility experience implantation failure while others do not.

PIEZO2 has predominantly been studied in sensory tissues, where its expression is orders of magnitude higher than in non-neuronal organs[86]. In the uterus, the low basal expression of PIEZO2 (~1/20,000 of dorsal root ganglia) initially seemed inconsistent with a functional role. However, PIEZO2 is dynamically induced by mechanical stimuli and is specifically localized to stromal cells, consistent with a stress-responsive function. This paradigm—low basal expression coupled with stimulus-dependent upregulation—is shared by many stress-responsive genes[87] and may reflect an adaptive strategy that limits constitutive signaling while enabling rapid responses to environmental challenges.

The clinical relevance of this mechanism is underscored by reduced PIEZO2 and PGR expression in endometrial samples from patients with RIF[88] and by the conservation of this signaling axis in human ESCs. Our findings provide a mechanistic link between abnormal uterine mechanics and defective progesterone signaling, suggesting that targeting mechanotransduction pathways—for instance, through modulation of collagen deposition, FAK activity, or Hippo signaling—may represent a potential therapeutic strategy for patients with implantation failure associated with uterine hypercontractility. We acknowledge that the human data presented here are derived from a limited cohort (n = 8 RIF and n = 8 fertile patients) and should be considered preliminary evidence. Validation in larger, prospectively enrolled cohorts with a standardized stress assessments will be essential to establish the clinical significance of the PIEZO2-PGR axis in RIF. More broadly, this study establishes that endocrine regulation of implantation is itself mechanically gated, revealing a fundamental convergence of mechanical and hormonal signaling in mammalian reproduction.

In summary, our findings support a mechanism where stress-induced uterine contractions generate mechanical signals that are sensed by PIEZO2 in endometrial stromal cells. This activates a collagen-dependent FAK-Hippo-YAP pathway that promotes PGR transcription and sustains progesterone responsiveness, thereby preserving implantation competence under stress. These findings establish a mechanosensing mechanism that buffers uterine function and reveals a fundamental link between mechanical forces and endocrine regulation in reproduction.

Methods

Patients and sample collection

All human samples were obtained from the Reproductive Medicine Center, Renmin Hospital, Hubei University of Medicine, Shiyan, Hubei Province, China with the approval of the Institutional Committee on the Use of Human Subjects of Hubei University of Medicine (No. SYSRMYY-KYXS-2026-022). Written informed consent was obtained prior to collecting residual endometrial biopsy specimen and corresponding serum samples for analysis. Two cohorts were examined in this study, an RIF cohort (n = 8; age range, 27–38 years), defined as unsuccessful clinical implantation following transfer of at least three morphologically good-quality embryos in two or more embryo transfer cycles, and a fertile control cohort (n = 8, age range, 29–39 years) requiring *in vitro* fertilization strictly due to mechanical fallopian tube obstruction (**Extended data Table 2**). Both cohorts completed a hormone replacement therapy (HRT) cycle. Once optimal endometrial thickness was confirmed via ultrasound, exogenous progesterone was administered and matched sample were collected exactly 5 days later (P + 5) to capture the window of implantation (WOI). Women with the following conditions were excluded from this study: recent contraception (intrauterine device and/or hormonal contraceptive use in the past three months); endocrine metabolic abnormalities, such as polycystic ovary syndrome, diabetes, insulin resistance, and hypothyroidism; genetic abnormalities; severe adenomyosis or endometriosis; severe hydrosalpinx; moderate to severe intrauterine adhesions; uterine malformations; recurrent miscarriage; thrombosis; autoimmune diseases; and body mass index (BMI) > 30.

Mice strains

Pgr$^{Cre/+}$ mice were kindly provided by Dr. FJ DeMayo and Dr. JP Lydon at Baylor College of Medicine, USA and floxed *Piezo1*$^{f/f}$ (Strain # 029213) and *Piezo2*$^{f/f}$ mice (Strain #027720) were purchased from The Jackson Laboratory. All animals were maintained under a 12 h light/dark cycle at approximately 22 °C with *ad libitum* access to food and water. To generate conditional knockout mice, *Pgr*$^{Cre/+}$ males were crossed with *Piezo2*$^{f/f}$ females, producing *Pgr*$^{Cre/+}$*Piezo2*$^{f/f}$ (*Piezo2*$^{d/d}$) and *Pgr*$^{+/+}$*Piezo2*$^{f/f}$ (*Piezo2*$^{f/f}$) littermates. In *Piezo2*$^{d/d}$ females, the *Piezo2* gene was specifically ablated in the endometrial compartment. The *Pgr*$^{Cre/+}$*Piezo1*$^{f/f}$ (*Piezo1*$^{d/d}$) and *Piezo1*$^{f/f}$ (*Piezo1*$^{f/f}$) mice were generated using the same strategy. Eight-week-old female mice were used in this study. All animal procedures were approved by the Institutional Animal Care and Use Committee of South China Agricultural University (2024b159) and complied with the Association for Assessment and Accreditation of Laboratory Animal Care International

(AAALAC).

Embryo implantation assessment and noise exposure in mice

Female mice were mated with fertile males of same strain (*Piezo2*$^{f/f}$), with a vaginal plug (0.5 dpc) deemed a successful mating. A subset was utilized to evaluate pre-implantation development (0.5−3.5 dpc) by flushing embryos from the oviducts or uterine horns. The remaining subset was evaluated at 4.5 dpc and implantation sites were visualized by intravenous injection of 1% Chicago Sky Blue (Sigma-Aldrich, # C8679) 5 min before euthanasia. Uterine horns were collected and examined, with implantation sites counted. In mice that exhibited implantation failure, samples were flushed to detect the presence of unattached, hatched blastocysts. Selected samples were fixed in 4% paraformaldehyde or snap frozen for further analyses.

To evaluate the effect of stress, plug-positive females were randomly assigned to a low-noise-quiet control group (45 ± 5 dB) or a high-noise exposure group (65 ± 5 dB) from 1.5 to 4.5 dpc. Intermittent high-noise exposure was performed for 12 h per day (8:00 a.m.–8:00 p.m.), while control mice were housed under low-noise conditions during the same time period.

Single prolonged stress (SPS)

To assess the impact of continuous maternal stress on early pregnancy, a modified Single Prolonged Stress (SPS) protocol was performed as previously described[46,89]. Briefly, pregnant female mice (0.5 dpc) underwent daily (applied at 9:00 a.m.) sequential stressors until reaching the 3.5 dpc stage. These included a 1.5 h restraint, 10 min forced swimming in 24 °C water, and a 15 min recovery period, followed by exposure to diethyl ether until loss of consciousness. Additionally, in a separate study cohort, Progesterone (P_4, 10mg/0.1mL) or vehicle (sesame oil) was administered intraperitoneally twice per day at 2.5 and 3.5 dpc at 12:00 p.m. and 5:00 p.m. For each study set, uteri from one subset were collected at 3.5 dpc for immediate blastocyst analysis, while implantation success was evaluated in a separate subset at 4.5 dpc.

Reciprocal embryo transfer

To isolate the tissue specific role of Piezo2, blastocysts were collected from either SPS-treated *Piezo2*$^{d/d}$ or *Piezo2*$^{f/f}$ donors and transferred into 3.5 dpc pseudopregnant, SPS-treated recipients of the reciprocal genotype at 11:00 a.m. Pseudopregnancy in recipient females was induced by mating with vasectomized males. Blastocysts (n = 4) were non-surgically introduced into a single uterine horn using a transcervical

embryo transfer device (College of Animal Science and Technology, Hebei Agricultural University, #AUH112015). The daily SPS protocol was continued for an additional two days, and implantation was evaluated at 5.5 dpc via intravenous injection of 1% Chicago Sky Blue dye (Sigma-Aldrich, # C8679).

Measurement of hormone levels

In mice, serum estradiol (E_2) and progesterone (P_4) levels were quantified using enzyme immunoassays (Shanghai Yanhui Biotechnology Co., Ltd.). Cortisol, epinephrine, and noradrenaline concentrations were measured using a human cortisol enzyme-linked immunosorbent assay (ELISA) kit (ADSBIO, #ADS-002002, ADS-640202, and ADS-545102, respectively) according to the manufacturer's protocols. For patient serum, cortisol, epinephrine, and noradrenaline concentrations were measured using a human cortisol enzyme-linked immunosorbent assay (ELISA) kit (Solarbio, #SEKSM-0071, SEKSM-0019, and SEKSM-0020, respectively) according to the manufacturer's protocols. All samples were assayed in duplicate, and cortisol concentrations were calculated based on a standard curve.

Pharmacological inhibition of Hippo signaling *in vivo*

The LATS1/2 inhibitor TDI-011536 (TDI; Selleck, # E1314) was dissolved in vehicle (10% Kolliphor HS 15 in PBS; Sigma-Aldrich, #42966)[90] and administered to SPS-treated *Piezo2*$^{d/d}$ mice by intraperitoneal injection at a dose of 100 mg/kg body weight, once daily from 1.5 to 3.5 dpc. Control mice (SPS-*Piezo2*$^{f/f}$) received an equivalent volume and duration of vehicle. Implantation was assessed at 4.5 dpc as described above.

***In vivo* NOS inhibition and quantification**

To inhibit nitric oxide synthase (NOS) activity *in vivo*, pregnant mice received intraperitoneal injections of Nω-Nitro-L-arginine methyl ester hydrochloride (L-NAME HCl; Selleck, #S287704) at a dose of 10 mg/kg body weight dissolved in sterile saline, administered once daily from 0.5 to 3.5 dpc. Control mice received an equal volume of sterile saline. A subset from each group was evaluated on 3.5 dpc for NOS activity within the uterine tissues, with implantation sites assessed on 4.5 dpc by intravenous injection of 1% Chicago Sky Blue dye.

NOS activity in endometrial tissues was measured at 3.5 dpc using a NOS Activity Assay Kit (Beyotime, #S0025) according to the manufacturer's instructions. Briefly, endometrial tissues were homogenized in the supplied lysis buffer and centrifuged to obtain a supernatant. NOS catalyzes the conversion of L-

arginine to L-citrulline and NO. The NO produced was quantified colorimetrically via the Griess reaction by measuring nitrite accumulation, with absorbance recorded at 540 nm on a microplate reader (BioTek Instruments, #ELX808), and NOS activity was normalized to the total protein concentration as determined by a BCA Protein Assay Kit (Thermo, #23227).

In vivo prostaglandin F2α administration

To induce uterine contractions *in vivo*, pregnant mice received subcutaneous injections of prostaglandin F2α (PGF2α; Aladdin, # D136300) at 1 mg/kg body weight dissolved in sterile PBS, administered once daily from 0.5 to 3.5 dpc. Control mice received an equal volume of sterile PBS. Uterine tissues were collected at 4.5 dpc and implantation was assessed.

Measurement of *ex vivo* uterine contraction

Mouse uteri were collected on 3.5 dpc and placed in 1 × PBS at 37 °C. Longitudinal uterine strips (~1 cm) were mounted in an organ bath containing carbogenated Krebs solution (119 mM NaCl, 4.7 mM KCl, 25 mM $NaHCO_3$, 1.2 mM KH_2PO_4, 2.5 mM $CaCl_2$, 1.5 mM $MgSO_4$, 11 mM glucose), maintained at 37 °C and continuously aerated (95% O_2, 5% CO_2) to maintain pH 7.4. One end of each strip was secured with a hook, while the opposite side was connected to an isometric force transducer under a resting tension of 1 g. Tissues were equilibrated for 30 min, followed by recording contractile activity for 30 min using the BL-420S Biological Data Acquisition & Analysis System (Chengdu TME Technology Co., Ltd., China). Spontaneous contractility was quantified by measuring contraction frequency (min^{-1}), amplitude (g), area under the curve (g·s), and contraction tension (g). To evaluate the effect of L-NAME HCl or $PGF_2\alpha$ on contraction, concentrations consistent with the experimental design described above were added to the carbogenated Krebs solution. To assess the impact of SPS on uterine contractility, uterine tissues were collected on 3.5 dpc in untreated control mice or SPS-treated mice (0.5-3.5 dpc) and *ex vivo* contractile responses were recorded as described above.

Ex vivo uterine stretch culture

Uteri from 3.5 dpc mice were collected, and the mesometrium, adipose tissue, and cervix were carefully removed under a dissecting microscope in ice-cold PBS. Each uterus was bisected longitudinally along the mesometrial boarder. One half was stretched to twice its original length and pinned to a culture dish, while the contralateral half was pinned without tension to serve as an unstretched control. Tissues were

incubated in DMEM/F12 (Sigma-Aldrich, #D2906) supplemented with 10% FBS (Excell Bio, #FSP500) and 1% penicillin/streptomycin (Gibco, #15140122) at 37 °C in 5% CO_2. Samples were harvested at 1, 6 or 12 h post-stretching and snap-frozen for downstream analyses.

Isolation of primary mouse endometrial stromal cells (MESCs)

Prior to cell isolation, 12-well culturing dishes were coated with type I collagen (Solarbio, # C8062) at 10 μg/cm^2 and incubated overnight at 4 °C. Excess collagen was removed the following day, and the culturing dishes were dried under ultraviolet (UV) irradiation overnight. Coated dishes were rinsed with sterile balanced salt solution prior to cell seeding. Uterine horns were extracted from 3.5 dpc pregnant mice, bisected longitudinally and digested in Hanks' balanced salt solution (HBSS) containing 1% trypsin (Amresco, #0458) and 6 mg/mL dispase II (Roche, #85022000). Luminal epithelial cells were removed, and the remaining tissue was rinsed in HBSS prior to being subjected to stromal digestion in HBSS containing 0.15 mg/mL collagenase I (Gibco, #17100-017). The isolated primary MESCs were then seeded onto the collagen coated culture dishes and maintained in DMEM/F12 medium supplemented with 10% FBS and 1% penicillin/streptomycin at 37 °C in a humidified incubator with 5% CO_2.

Decidualization induced in a human endometrial stromal cell (T-HESC) line

A human endometrial stromal cell (T-HESC) line (ATCC, # CRL-4003) was maintained in DMEM/F12 supplemented with 10% FBS, 100 U/mL penicillin, and 0.1 mg/mL streptomycin (Procell, # PB180429) at 37 °C in 5% CO_2. Upon reaching 70% confluency, decidualization was induced by replacing the maintenance media with DMEM/F12 supplemented with 2% charcoal-stripped FBS (VivaCell, #C3830), 1 μM medroxyprogesterone acetate (MedChemExpress, # HY-B0469), and 0.1 mM db-cAMP (Sigma-Aldrich, # D0627). Decidualization conditions were maintained for 4 d, with media refreshed every 2 days.

IGF1 supplementation in MESCs

Primary MESCs were isolated as described above and cultured in DMEM/F12 medium supplemented with 10% FBS. When cells reached approximately 70% confluence, the medium was replaced with serum-free DMEM/F12 for 12 h to achieve serum starvation. The cells were then incubated with fresh serum-free DMEM/F12 containing 100 ng/mL IGF1 (MedChemExpress, # HY-P7070) for 24 h. Total RNA was extracted and subjected to quantitative RT-PCR analysis.

Pharmacological inhibitors

The following inhibitors were used in cell culture experiments: BAPTA-AM (Ca^{2+} chelator; Selleck, #S7534, 10 μM), KN93 (CaMKII phosphorylation inhibitor; Selleck, #S6787, 10 μM), Y15 (FAK phosphorylation inhibitor; Selleck, # S5321, 10 μM), Verteporfin (YAP–TEAD interaction inhibitor; Selleck, #S1786, 2 μM), TDI-011536 (TDI; LATS1/2 inhibitor; Selleck, #E1314, 3 μM). All inhibitors were dissolved in DMSO, and an equal volume of DMSO was used as vehicle control.

8×GTIIC TEAD reporter assay

To examine YAP–TEAD transcriptional activity, primary MESCs were cultured onto either COL-I-coated or uncoated dishes. Upon reaching 70% confluency, cells were co-transfected with 1 μg of 8×GTIIC luciferase reporter plasmid (containing eight copies of the TEAD-responsive element; Addgene, #34615) and 100 ng of pRL-SV40 Renilla luciferase control plasmid (Beyotime, # D2768) using Lipofectamine 2000 (Invitrogen, #11668019). After culturing for 48 h, the cells were lysed and luciferase activity was quantified using a Dual-Luciferase Reporter Assay Kit (Beyotime, # RG027). Firefly luciferase activity was normalized to Renilla luciferase to account for transfection efficiency variations.

Collagen coating densities

To evaluate the effect of the COL-I matrix density on *Piezo2* and *Pgr*, primary MESCs or T-HESCs were cultured on dishes coated with 0, 10, 20, or 40 μg/cm^2 of COL-I (C8061, Solarbio) as described in the 'Isolation of primary mouse endometrial stromal cells (MESCs)' section. Total RNA was then extracted, and relative mRNA was determined using quantified RT-PCR.

PIEZO2 knockdown and PGR overexpression in human ESC cell (T-HESC) line

For siRNA-mediated PIEZO2 knockdown, T-HESCs were transfected with non-targeting (Scrambled) control siRNA or human PIEZO2 siRNAs (Ribobio, China; **Extended data Table 3**) using Lipofectamine 2000 (11668019, Invitrogen) for 6 h according to the manufacturer's protocols. To examine overexpression, human *PGR-A* or *PGR-B* cDNA was cloned into pcDNA3.1 vectors (kindly provided by Dr. Wen-Bo Deng, Xiamen University, Xiamen, China). Cells were seeded (1×10^5 cells) in a 35 mm dish and transiently transfected with 2 μg of pcDNA3.1-*PGR-A*, pcDNA3.1-*PGR-B* or pcDNA3.1 plasmids using Lipofectamine 2000 according to the manufacturer's instructions. All cells were harvested 48 h post-transfection for analysis.

Histological analysis and immunostaining

Paraffin-embedded uterine tissues were sectioned (5 μm), deparaffinized with xylene, and rehydrated through a graded ethanol series prior to hematoxylin and eosin (H&E) staining for histological analysis. For immunohistochemistry, sections underwent antigen retrieval in sodium citrate buffer (pH 6.0), followed by endogenous peroxidase quenching with 3% hydrogen peroxide. After blocking with 10% normal goat serum, sections were incubated with primary antibodies, followed by the addition of biotinylated secondary antibodies (**Extended data Table 4**). Sections were then incubated with Streptavidin–Horseradish Peroxidase conjugate (Invitrogen, cat.
#434323) for 30 min at room temperature, and immunoreactive signals were visualized using 3,3'-diaminobenzidine (DAB) substrate (Vector Laboratories, cat. #SK-4100). Sections were then counterstained with hematoxylin, dehydrated through a graded ethanol series, cleared in xylene and mounted with coverslips for imaging.

Frozen uterine tissues were embedded in OCT compound, cryosectioned (10 μm), and fixed in 4% paraformaldehyde (PFA) for 1 h at room temperature. Sections were then blocked in 5% BSA in PBS-T (0.1% Triton X-100) and incubated overnight at 4 °C with primary antibodies (**Extended data Table 4**). Samples were then washed and incubated with Alexa Fluor 488–conjugated goat anti-rabbit IgG (Invitrogen, # A11008). Nuclei were counterstained with DAPI (Thermo Fisher, # D21490) and images were captured using a Leica TCS SP8 microscope.

Masson's trichrome staining

Paraffin-embedded uterine sections (5 μm) were deparaffinized in xylene, rehydrated through a graded ethanol series, and stained using a Masson's Trichrome Stain Kit (Solarbio, # G1340) according to the manufacturer's instructions. Cell nuclei were stained with iron hematoxylin, muscle fibers with Ponceau magenta, and collagen fibers with aniline blue. Sections were subsequently dehydrated, cleared with xylene, and mounted with coverslips for imaging.

Fluorescent *in situ* hybridization

Single-molecule fluorescence *in situ* hybridization (smFISH) was performed following the SCRINSHOT protocol[91]. Frozen tissue sections were first fixed in 4% PFA for 1 h and subsequently blocked in a buffer containing 0.1 μM oligo(dT)s (Sangon Biotech) and 0.2 μg/μl tRNA (Solarbio, # T8630). Target hybridization was carried out using 0.1 μM padlock probes (Sangon Biotech) that were first denatured at

55 °C for 15 min and then hybridized to the target RNA during an incubation at 45 °C for 4 h. The annealed padlock probes were then circularized using 0.5 U/μl SplintR ligase (NEB, # M0375) at 37 °C for 1 h. Rolling circle amplification (RCA) was performed overnight at 25 °C using a thiophosphate-modified RCA primer (0.1 μM; Takara Bio, #5017, Mfg.ID: CJSY248-01) and ϕ29 DNA polymerase (0.5 U/μl; Themo Fisher, # EP0091). The resulting RCA products were incubated with an HRP-conjugated detection probe (0.04 μM; Takara Bio, #5018, Mfg.ID: CJMY249-01) and visualized using tyramide signal amplification (TSA, 1:500; Servicebio, #G1231) according to the manufacturer's instructions. Images were acquired using a Leica TCS SP8 confocal microscope (Leica, Germany). The oligo(dT), padlock probe, and RCA primer sequences are listed in **Extended data Table 3**.

Western blot

Tissues were lysed in RIPA buffer (Yamei, # PC101), and protein concentrations were determined using a Pierce™ BCA Protein Assay Kit (Thermo Fisher, #1859078). Proteins (10 μg per lane) were resolved on 10% SDS–PAGE gels and transferred to 0.45 μm nitrocellulose membranes (Millipore, # ISEQ00010). The membranes were blocked with 5% non-fat milk for 1 h at room temperature and incubated with primary antibodies at 4 °C overnight. Samples were then washed and incubated with HRP-conjugated secondary antibodies. Immunoreactive bands were visualized using enhanced chemiluminescence (Seyotin, # STP262) and imaged on a Tanon-5200 system (Tanon, Shanghai, China). All antibodies are listed in **Extended data Table 4**.

PGR dual-luciferase reporter assay

To construct the luciferase reporter plasmid, a wild-type mouse *Pgr* promoter fragment spanning -200 to +50 bp relative to the transcription start site (TSS), containing a predicted TEAD binding motif (ATATTCCAG) at −138 to −127 bp, or a corresponding mutant (ATATTCCAG to ATGAGTAAG) was synthesized, and cloned into a pGL3 vector following restriction enzyme digestion (Sangon Biotech) to generate wild-type (pGL3-*Pgr*) or mutant (pGL3-*Pgr*-mutant) plasmids, respectively. MESCs were then co-transfected with either pGL3-*Pgr* or pGL3-*Pgr*-mutant and a pRL-SV40 plasmid (Beyotime, #D2768) using Lipofectamine 3000 according to the manufacturer's instructions. Following a 48h incubation, cells were lysed and luciferase activity was measured using a Dual-Luciferase Reporter Assay Kit (Beyotime, # RG027) according to the manufacturer's instructions. The Firefly luciferase signal was normalized to the corresponding *Renilla* luciferases activity to calculate a relative activity.

RNA isolation and quantitative real-time PCR

Total RNA was extracted from tissues or cells using TRIzol reagent (Takara, #AG21102) according to the manufacturer's instructions. RNA purity and concentration were determined via spectrophotometry. First-strand cDNA was synthesized from 1 μg of total RNA using a HiSuperscript cDNA Synthesis Kit (Vazyme, #R222-01) according to the manufacture's protocols. Quantitative RT-PCR was performed using SYBR qPCR Master Mix (Vazyme, #Q311-02) on a Bio-Rad CFX96 Real-Time PCR Detection System (Bio-Rad, USA). Gene expression was normalized to mouse *Rpl19* or human *GAPDH*, and relative transcript levels were quantified using the $2^{-\Delta\Delta Ct}$ method. Primer sequences are listed in **Extended data Table 3**, and all samples were examined in triplicate.

Single-cell RNA sequencing of mouse uteri

Uteri were collected from SPS-treated *Piezo*$^{d/d}$ and *Piezo2*$^{f/f}$ female mice (n = 2 per genotype) on 3.5 dpc. After removal of the mesometrium, adipose tissue, and cervix, uteri were minced into ~1 mm pieces and enzymatically digested in DMEM containing collagenase II (160 U/mL; Worthington, #LS004176) and DNase I (7.5 μg/mL; Roche, #10104159001) at 37 °C for 60 min with gentle agitation. The resulting cell suspension was passed through a 40 μm cell strainer (Corning) and centrifuged at 400g for 5 min. Red blood cells were lysed on ice for 5 min with 1 mL Red Blood Cell Lysis Buffer (Roche, #11814389001). Dead cells were removed using a Dead Cell Removal Kit (Miltenyi Biotec, #130-090-101) according to the manufacturer's instructions. Cell number and viability (>85%) were assessed by 0.4% trypan blue exclusion.

Single-cell RNA sequencing (scRNA-seq) libraries were generated using the Chromium Next GEM Single Cell 3′ Gene Expression platform (10× Genomics, # CG000183) according to the manufacturer's protocols. Briefly, single-cell suspensions were loaded onto the Chromium Controller to generate single-cell gel beads in emulsion (GEMs) to facilitate barcoding and reverse transcription. Following cDNA amplification, gene expression libraries were prepared using Chromium Single Cell 3' Reagent Kits v3.1 (10× Genomics) according to the manufacturer's instructions. Libraries were quantified using a Qubit fluorometer (Thermo Fisher) and the library size distribution was assessed using an Agilent 2100 Bioanalyzer. Sequencing was performed on an Illumina Novaseq 6000 platform using 150-bp paired-end reads, targeting a minimum sequencing depth of 50,000 reads per cell. Raw sequencing data was deposited in the Gene Expression Omnibus (GEO) under accession number GSE285982.

Single-cell RNA sequencing data analysis

Raw FASTQ files were processed using the Cell Ranger pipeline (v5.0.1, 10X Genomics) with default parameters. Reads were aligned to the mouse reference genome (mm10) using the STAR aligner (v2.7.2a) integrated within Cell Ranger. The Cell Ranger cell-calling algorithm was used to identify valid cell barcodes based on total unique molecular identifier (UMI) counts and gene-by-barcode count matrices. Count matrices were then imported into R (v4.3.0) for downstream analysis using the Seurat package (v4.3.0).

Quality control. Low-quality cells were excluded if fewer than 200 or more than 2,500 genes were detected or greater than 5% mitochondrial gene expression. Genes expressed in fewer than three cells were removed. Potential doublets were identified and removed using DoubletFinder (v2.0.3). Briefly, optimal pK values were determined by pN–pK parameter sweeps, with the pK corresponding to the maximum mean-variance-normalized bimodality coefficient (BCmvn) selected. Homotypic doublet proportions were estimated from the sum of squared cell-type annotation frequencies, and the expected doublet rate was set based on the 10x Genomics loading guidelines. Cells identified as doublets (1.5–3.8% per sample) were excluded from further analysis.

Normalization and dimensionality reduction. UMI count data were normalized using the global-scaling 'LogNormalize' method in Seurat, with gene expression for each cell normalized to the total UMI count, multiplied by a scale factor of 10,000, and log-transformed. The top 1,500 highly variable genes were identified using the variance-stabilizing transformation (VST) method via the 'FindVariableFeatures' function and principal component analysis (PCA) was used for dimensionality reduction. The number of statistically significant principal components (PCs) was determined using the JackStraw permutation test, with the top 30 PCs selected for further analysis. Cells were visualized in two-dimensional space using Uniform Manifold Approximation and Projection (UMAP).

Clustering and cell-type annotation. A shared nearest-neighbor (SNN) graph was constructed based on the top 30 PCs, and cell clusters were detected using the Louvain community detection algorithm implemented in Seurat. Resolution parameters were optimized, with a resolution of 0.2 selected to ensure distinct cell populations were produced that were supported by canonical marker gene expression. Cell types were assigned based on the expression of established canonical marker genes and cross-referenced with published mouse uterine single-cell datasets. To resolve fibroblast heterogeneity, stromal fibroblasts were computationally subset from the full dataset and re-clustered using the same pipeline.

Differential gene expression analysis. Differentially expressed genes (DEGs) between clusters or experimental conditions were identified using the 'FindMarkers' function in Seurat and statistical significance was determined using a Wilcoxon rank-sum test. Genes were considered significantly differentially expressed if they exhibited a Bonferroni-adjusted $P < 0.01$, average $\log^2$ fold change ≥ 0.5, and detection in > 25% of cells in the relevant cluster. For comparisons between genotypes (SPS-*Piezo2*-cKO versus SPS-*Piezo2* control), DEGs were computed within each annotated cell type independently.

Gene Ontology and pathway enrichment analysis. Functional enrichment analysis of DEGs was performed using Gene Ontology (GO) and Kyoto Encyclopedia of Genes and Genomes (KEGG) databases. Enrichment significance was assessed using the hypergeometric test, and *P* values were adjusted for multiple testing using the Benjamini–Hochberg method. GO terms and KEGG pathways with a false discovery rate (FDR) ≤ 0.05 were considered significantly enriched.

Ligand–receptor interaction analysis

Cell–cell communication networks were inferred using CellPhoneDB (v2.0.0; https://github.com/Teichlab/cellphonedb). The normalized scRNA-seq count matrix and cell-type annotations were used as inputs. Ligand–receptor interaction enrichment was computed against the default curated database using 1,000 permutations, with interactions deemed statistically significant at $P \leq 0.05$. Interaction strength was quantified as the $\log^2$-transformed mean of the average expression values for the corresponding ligand–receptor pair within the interacting cell types. Significant interactions between stromal fibroblast subclusters and involving the IGF signaling pathway were extracted and visualized using dot plots and chord diagrams generated with custom R scripts.

Statistical analysis

Statistical comparisons between two groups were performed using a two-tailed Student's *t*-test, while multiple-group comparisons were conducted using a two-way ANOVA followed by an appropriate post hoc test. All analyses were carried out in GraphPad Prism 10.0 (GraphPad Software), with all data presented as mean ± SEM and $P < 0.05$ deemed statistically significant.

References

1 Ombelet, W., Cooke, I., Dyer, S., Serour, G. & Devroey, P. Infertility and the provision of infertility medical services in developing countries. *Hum Reprod Update* **14**, 605-621 (2008). https://doi.org/10.1093/humupd/dmn042

2 Wang, H. & Dey, S. K. Roadmap to embryo implantation: clues from mouse models. *Nat Rev Genet* **7**, 185-199 (2006). https://doi.org/10.1038/nrg1808

3 Cha, J., Sun, X. & Dey, S. K. Mechanisms of implantation: strategies for successful pregnancy. *Nat Med* **18**, 1754-1767 (2012). https://doi.org/10.1038/nm.3012

4 Gellersen, B. & Brosens, J. J. Cyclic decidualization of the human endometrium in reproductive health and failure. *Endocr Rev* **35**, 851-905 (2014). https://doi.org/10.1210/er.2014-1045

5 Mulac-Jericevic, B., Mulac-Jericevic, R. A., DeMayo F.J., Lydon J.P. & Conneely O.M. Subgroup of reproductive functions of progesterone mediated by progesterone receptor-B isoform. *Science* **289**, 1751-1754 (2000). https://doi.org/doi:10.1126/science.289.5485.1751

6 DeMayo, F. J. & Lydon, J. P. 90 YEARS OF PROGESTERONE: New insights into progesterone receptor signaling in the endometrium required for embryo implantation. *J Mol Endocrinol* **65**, T1-T14 (2020). https://doi.org/10.1530/JME-19-0212

7 Patel, B. *et al.* Role of nuclear progesterone receptor isoforms in uterine pathophysiology. *Hum Reprod Update* **21**, 155-173 (2015). https://doi.org/10.1093/humupd/dmu056

8 Ijland, M. M., Evers, J. L., Dunselman, G. A. & Hoogland, H. J. Endometrial wavelike activity, endometrial thickness, and ultrasound texture in controlled ovarian hyperstimulation cycles. *Fertil Steril* **70**, 279-283 (1998). https://doi.org/10.1016/s0015-0282(98)00132-0

9 Chen, Q. *et al.* Transient beta2-adrenoceptor activation confers pregnancy loss by disrupting embryo spacing at implantation. *J Biol Chem* **286**, 4349-4356 (2011). https://doi.org/10.1074/jbc.M110.197202

10 Kunz, G., Herbertz, M., Noe, M. & Leyendecker, G. Sonographic evidence for the involvement of the utero-ovarian counter-current system in the ovarian control of directed uterine sperm transport. *Hum Reprod Update* **4**, 667-672 (1998). https://doi.org/10.1093/humupd/4.5.667

11 Kunz, G., Beil, D., Deininger, H., Wildt, L. & Leyendecker, G. The dynamics of rapid sperm transport through the female genital tract: evidence from vaginal sonography of uterine peristalsis and hysterosalpingoscintigraphy. *Hum Reprod* **11**, 627-632 (1996). https://doi.org/10.1093/humrep/11.3.627

12 Kunz, G., Noe, M., Herbertz, M. & Leyendecker, G. Uterine peristalsis during the follicular phase of the menstrual cycle: effects of oestrogen, antioestrogen and oxytocin. *Hum Reprod Update* **4**, 647-654 (1998). https://doi.org/10.1093/humupd/4.5.647

13 Ferraretti, A. P. *et al.* Assisted reproductive technology in Europe, 2009: results generated from European registers by ESHRE. *Hum Reprod* **28**, 2318-2331 (2013). https://doi.org/10.1093/humrep/det278

14 Fanchin, R. *et al.* Uterine contractility decreases at the time of blastocyst transfers. *Hum Reprod* **16**, 1115-1119 (2001). https://doi.org/10.1093/humrep/16.6.1115

15 Lesny, P., Maguiness, S., Biervliet, F. & Killick, S. R. Uterine contractility decreases at the time of blastocyst transfer. *Hum Reprod* **17**, 841 (2002). https://doi.org/10.1093/humrep/17.3.841

16 Fanchin, R. *et al.* Effects of vaginal progesterone administration on uterine contractility at the time of embryo transfer. *Fertil Steril* **75**, 1136-1140 (2001). https://doi.org/10.1016/s0015-0282(01)01787-3

17 Fujii, O. *et al.* Uterine relaxation by sacral surface electrical stimulation on the day of embryo transfer. *Fertil Steril* **90**, 1240-1242 (2008). https://doi.org/10.1016/j.fertnstert.2007.08.059

18 Lan, V. T., Khang, V. N., Nhu, G. H. & Tuong, H. M. Atosiban improves implantation and pregnancy rates in patients with repeated implantation failure. *Reprod Biomed Online* **25**, 254-260 (2012). https://doi.org/10.1016/j.rbmo.2012.05.014

19 Fanchin, R. *et al.* Uterine contractions at the time of embryo transfer alter pregnancy rates after in-vitro fertilization. *Hum Reprod* **13**, 1968-1974 (1998). https://doi.org/10.1093/humrep/13.7.1968

20 He, Y. *et al.* Administration of atosiban in patients with endometriosis undergoing frozen-thawed embryo transfer: a prospective, randomized study. *Fertil Steril* **106**, 416-422 (2016). https://doi.org/10.1016/j.fertnstert.2016.04.019

21 Bulletti, C. *et al.* Myomas, pregnancy outcome, and in vitro fertilization. *Ann N Y Acad Sci* **1034**, 84-92 (2004). https://doi.org/10.1196/annals.1335.010

22 Lynch, C. D., Sundaram, R., Maisog, J. M., Sweeney, A. M. & Buck Louis, G. M. Preconception stress increases the risk of infertility: results from a couple-based prospective cohort study--the LIFE study. *Hum Reprod* **29**, 1067-1075 (2014). https://doi.org/10.1093/humrep/deu032

23 Louis, G. M. *et al.* Stress reduces conception probabilities across the fertile window: evidence in support of relaxation. *Fertil Steril* **95**, 2184-2189 (2011). https://doi.org/10.1016/j.fertnstert.2010.06.078

24 Dole, N. *et al.* Maternal stress and preterm birth. *Am J Epidemiol* **157**, 14-24 (2003). https://doi.org/10.1093/aje/kwf176

25 Wdowiak, A. *et al.* Interactions of Cortisol and Prolactin with Other Selected Menstrual Cycle Hormones Affecting the Chances of Conception in Infertile Women. *Int J Environ Res Public Health* **17** (2020). https://doi.org/10.3390/ijerph17207537

26 Palomba, S., Daolio, J., Romeo, S., Battaglia, F.A., Marber, R. & La Sala, G.B. Lifestyle and fertility: the influence of stress and quality of life on female fertility. *Reprod. Biol. Endocrinol.* **16**, 113 (2018). https://doi.org/10.1186/s12958-018-0434-y

27 Robertson, E. M. The Effects of Emotional Stress on the Contractions of the Human Uterus. *BJOG* **46**, 741–747 (1939). https://doi.org/10.1111/j.1471-0528.1939.tb05374.x

28 Pribek, I. K. *et al.* Detection of acute stress by smooth muscle electromyography: A translational study on rat and human. *Life Sci* **277**, 119492 (2021). https://doi.org/10.1016/j.lfs.2021.119492

29 Coste, B. *et al.* Piezo1 and Piezo2 are essential components of distinct mechanically activated cation channels. *Science* **330**, 55-60 (2010). https://doi.org/10.1126/science.1193270

30 Li, J. *et al.* Piezo1 integration of vascular architecture with physiological force. *Nature* **515**, 279-282 (2014). https://doi.org/10.1038/nature13701

31 Wang, L. *et al.* Mechanical sensing protein PIEZO1 regulates bone homeostasis via osteoblast-osteoclast crosstalk. *Nat Commun* **11**, 282 (2020). https://doi.org/10.1038/s41467-019-14146-6

32 Romac, J. M., Shahid, R. A., Swain, S. M., Vigna, S. R. & Liddle, R. A. Piezo1 is a mechanically activated ion channel and mediates pressure induced pancreatitis. *Nat Commun* **9**, 1715 (2018). https://doi.org/10.1038/s41467-018-04194-9

33 Friedrich, E. E. *et al.* Endothelial cell Piezo1 mediates pressure-induced lung vascular hyperpermeability via disruption of adherens junctions. *Proc Natl Acad Sci U S A* **116**, 12980-12985 (2019).

https://doi.org/10.1073/pnas.1902165116

34 Atcha, H. *et al.* Mechanically activated ion channel Piezo1 modulates macrophage polarization and stiffness sensing. *Nat Commun* **12**, 3256 (2021). https://doi.org/10.1038/s41467-021-23482-5

35 Choi, D. *et al.* Piezo1-Regulated Mechanotransduction Controls Flow-Activated Lymphatic Expansion. *Circ Res* **131**, e2-e21 (2022). https://doi.org/10.1161/CIRCRESAHA.121.320565

36 Solis, A. G. *et al.* Mechanosensation of cyclical force by PIEZO1 is essential for innate immunity. *Nature* **573**, 69-74 (2019). https://doi.org/10.1038/s41586-019-1485-8

37 Baghdadi, M. B. *et al.* PIEZO-dependent mechanosensing is essential for intestinal stem cell fate decision and maintenance. *Science* **386**, eadj7615 (2024). https://doi.org/10.1126/science.adj7615

38 Barnett, S. D., Asif, H. & Buxton, I. L. O. Novel identification and modulation of the mechanosensitive Piezo1 channel in human myometrium. *J Physiol* **601**, 1675-1690 (2023). https://doi.org/10.1113/JP283299

39 Zhang, Y. *et al.* PIEZO channels link mechanical forces to uterine contractions in parturition. *Science* **390**, eady3045 (2025). https://doi.org/10.1126/science.ady3045

40 Ranade, S. S. *et al.* Piezo2 is the major transducer of mechanical forces for touch sensation in mice. *Nature* **516**, 121-125 (2014). https://doi.org/10.1038/nature13980

41 Florez-Paz, D., Bali, K. K., Kuner, R. & Gomis, A. A critical role for Piezo2 channels in the mechanotransduction of mouse proprioceptive neurons. *Sci Rep* **6**, 25923 (2016). https://doi.org/10.1038/srep25923

42 Bi, Y. *et al.* Piezo1 overexpression in the uterus contributes to myometrium contraction and inflammation-associated preterm birth. *J Transl Med* **22**, 1140 (2024). https://doi.org/10.1186/s12967-024-05978-y

43 Zhang, Y. *et al.* PIEZO channels link mechanical forces to uterine contractions in parturition. *Science* **390**, eady3045 (2025). https://doi.org/10.1126/science.ady3045

44 Sanchez-Rubio, M. *et al.* Maternal stress during pregnancy alters circulating small extracellular vesicles and enhances their targeting to the placenta and fetus. *Biol Res* **57**, 70 (2024). https://doi.org/10.1186/s40659-024-00548-4

45 Traylor, C. S., Johnson, J. D., Kimmel, M. C. & Manuck, T. A. Effects of psychological stress on adverse pregnancy outcomes and nonpharmacologic approaches for reduction: an expert review. *Am J Obstet Gynecol MFM* **2**, 100229 (2020). https://doi.org/10.1016/j.ajogmf.2020.100229

46 Coussons-Read, M. E. Effects of prenatal stress on pregnancy and human development: mechanisms and pathways. *Obstet Med* **6**, 52-57 (2013). https://doi.org/10.1177/1753495X12473751

47 Souza, R. R., Noble, L. J. & McIntyre, C. K. Using the Single Prolonged Stress Model to Examine the Pathophysiology of PTSD. *Front Pharmacol* **8**, 615 (2017). https://doi.org/10.3389/fphar.2017.00615

48 Yamamoto, S. *et al.* Effects of single prolonged stress and D-cycloserine on contextual fear extinction and hippocampal NMDA receptor expression in a rat model of PTSD. *Neuropsychopharmacology* **33**, 2108-2116 (2008). https://doi.org/10.1038/sj.npp.1301605

49 Kang, J.-W. *et al.* PIEZO1-mediated endometrial decidualization is disrupted in miscarriage through BECN1-dependent autophagy. *Communications Biology* (2026). https://doi.org/10.1038/s42003-026-10693-z

50 Dey, S. K. *et al.* Molecular cues to implantation. *Endocr Rev* **25**, 341-373 (2004). https://doi.org/10.1210/er.2003-0020

51 Kurita, T. *et al.* Stromal progesterone receptors mediate the inhibitory effects of progesterone on estrogen-induced uterine epithelial cell deoxyribonucleic acid synthesis. *Endocrinology* **139**, 4708-4713 (1998). https://doi.org/10.1210/endo.139.11.6317

52 Yallampalli, C., Izumi, H., Byam-Smith, M. & Garfield, R. E. An L-arginine-nitric oxide-cyclic guanosine monophosphate system exists in the uterus and inhibits contractility during pregnancy. *Am J Obstet Gynecol* **170**, 175-185 (1994). https://doi.org/10.1016/s0002-9378(94)70405-8

53 Sugimoto, Y. *et al.* Failure of parturition in mice lacking the prostaglandin F receptor. *Science* **277**, 681-683 (1997). https://doi.org/10.1126/science.277.5326.681

54 Miano, J. M., Cserjesi, P., Ligon, K. L., Periasamy, M. & Olson, E. N. Smooth muscle myosin heavy chain exclusively marks the smooth muscle lineage during mouse embryogenesis. *Circ Res* **75**, 803-812 (1994). https://doi.org/10.1161/01.res.75.5.803

55 Owens, G. K., Kumar, M. S. & Wamhoff, B. R. Molecular regulation of vascular smooth muscle cell differentiation in development and disease. *Physiol Rev* **84**, 767-801 (2004). https://doi.org/10.1152/physrev.00041.2003

56 Glasser, S. R. & Julian, J. Intermediate filament protein as a marker of uterine stromal cell decidualization. *Biol Reprod* **35**, 463-474 (1986). https://doi.org/10.1095/biolreprod35.2.463

57 Benson, G. V. *et al.* Mechanisms of reduced fertility in Hoxa-10 mutant mice: uterine homeosis and loss of maternal Hoxa-10 expression. *Development* **122**, 2687-2696 (1996). https://doi.org/10.1242/dev.122.9.2687

58 Curry, T. E., Jr. & Osteen, K. G. The matrix metalloproteinase system: changes, regulation, and impact throughout the ovarian and uterine reproductive cycle. *Endocr Rev* **24**, 428-465 (2003). https://doi.org/10.1210/er.2002-0005

59 Rausch, V. & Hansen, C. G. The Hippo Pathway, YAP/TAZ, and the Plasma Membrane. *Trends Cell Biol* **30**, 32-48 (2020). https://doi.org/10.1016/j.tcb.2019.10.005

60 Lan, Y. *et al.* Piezo1-Mediated Mechanotransduction Contributes to Disturbed Flow-Induced Atherosclerotic Endothelial Inflammation. *J Am Heart Assoc* **13**, e035558 (2024). https://doi.org/10.1161/JAHA.123.035558

61 Zhao, B. *et al.* TEAD mediates YAP-dependent gene induction and growth control. *Genes Dev* **22**, 1962-1971 (2008). https://doi.org/10.1101/gad.1664408

62 Castro-Mondragon, J. A. *et al.* JASPAR 2022: the 9th release of the open-access database of transcription factor binding profiles. *Nucleic Acids Res* **50**, D165-D173 (2022). https://doi.org/10.1093/nar/gkab1113

63 Wu, J. *et al.* Maternal anxiety affects embryo implantation via impairing adrenergic receptor signaling in decidual cells. *Commun Biol* **5**, 840 (2022). https://doi.org/10.1038/s42003-022-03694-1

64 Guo, Y. B., Tang, B., Zhang, L., Wu, X. & Huang, Z. H. Anxiety and depression in recurrent implantation failure after frozen-thawed embryo transfer and efficacy of endometrial receptivity testing. *World J Psychiatry* **15**, 109175 (2025). https://doi.org/10.5498/wjp.v15.i9.109175

65 Togher, K. L., Treacy, E., O'Keeffe, G. W. & Kenny, L. C. Maternal distress in late pregnancy alters obstetric outcomes and the expression of genes important for placental glucocorticoid signalling. *Psychiatry Res* **255**, 17-26 (2017). https://doi.org/10.1016/j.psychres.2017.05.013

66 Chen, M. *et al.* Association between pre-pregnancy maternal stress and small for gestational age: a population-based retrospective cohort study. *BMC Med* **23**, 7 (2025). https://doi.org/10.1186/s12916-024-03837-7

67 Vasquez, Y. M. *et al.* FOXO1 is required for binding of PR on IRF4, novel transcriptional regulator of endometrial stromal decidualization. *Mol Endocrinol* **29**, 421-433 (2015). https://doi.org/10.1210/me.2014-1292

68 Khairy, M., Dhillon, R. K., Chu, J., Rajkhowa, M. & Coomarasamy, A. The effect of peri-implantation administration of uterine relaxing agents in assisted reproduction treatment cycles: a systematic review and meta-analysis. *Reprod Biomed Online* **32**, 362-376 (2016). https://doi.org/10.1016/j.rbmo.2016.01.004

69 An, B. S. *et al.* Effects of estrogen and estrogenic compounds, 4-tert-octylphenol, and bisphenol A on the uterine contraction and contraction-associated proteins in rats. *Mol Cell Endocrinol* **375**, 27-34 (2013). https://doi.org/10.1016/j.mce.2013.04.025

70 Ozkaya, E. *et al.* Area under the curve of temporal estrogen and progesterone measurements during assisted reproductive technology: Which hormone is the main determinant of cycle outcome? *J Obstet Gynaecol Res* **44**, 263-269 (2018). https://doi.org/10.1111/jog.13492

71 Salmeri, N. *et al.* Functional determinants of uterine contractility in endometriosis and adenomyosis: a systematic review and meta-analysis. *Fertil Steril* **122**, 1063-1078 (2024). https://doi.org/10.1016/j.fertnstert.2024.07.026

72 Vidal, A. *et al.* Lower pregnancy rate in women with high uterine peristalsis before embryo transfer: a systematic review and meta-analysis. *Reprod Biol Endocrinol* **23**, 49 (2025). https://doi.org/10.1186/s12958-025-01380-5

73 Dittrich, R. *et al.* Differences in muscarinic-receptor agonist-, oxytocin-, and prostaglandin-induced uterine contractions. *Fertil Steril* **92**, 1694-1700 (2009). https://doi.org/10.1016/j.fertnstert.2008.08.117

74 Richter, O. N. *et al.* Oxytocin receptor gene expression of estrogen-stimulated human myometrium in extracorporeally perfused non-pregnant uteri. *Mol Hum Reprod* **10**, 339-346 (2004). https://doi.org/10.1093/molehr/gah039

75 Tyler, B. *et al.* Interventions to optimize embryo transfer in women undergoing assisted conception: a comprehensive systematic review and meta-analyses. *Hum Reprod Update* **28**, 480-500 (2022). https://doi.org/10.1093/humupd/dmac009

76 Pierzynski P., R. T. M., Kuczynski, W. Oxytocin antagonists may improve infertility treatment. *Fertility and Sterility.* **88**, 213.e219-213.e222 (2007). https://doi.org/10.1016/j.fertnstert.2006.09.017

77 Guo, S. W., Mao, X., Ma, Q. & Liu, X. Dysmenorrhea and its severity are associated with increased uterine contractility and overexpression of oxytocin receptor (OTR) in women with symptomatic adenomyosis. *Fertil Steril* **99**, 231-240 (2013). https://doi.org/10.1016/j.fertnstert.2012.08.038

78 Leyendecker, G., Herbertz, M., Kunz, G. & Mall, G. Endometriosis results from the dislocation of basal endometrium. *Hum Reprod* **17**, 2725-2736 (2002). https://doi.org/10.1093/humrep/17.10.2725

79 Leyendecker, G. *et al.* Uterine peristaltic activity and the development of endometriosis. *Ann N Y Acad Sci* **1034**, 338-355 (2004). https://doi.org/10.1196/annals.1335.036

80 Dupont, S. *et al.* Role of YAP/TAZ in mechanotransduction. *Nature* **474**, 179-183 (2011). https://doi.org/10.1038/nature10137

81 Meng, Z. *et al.* RAP2 mediates mechanoresponses of the Hippo pathway. *Nature* **560**, 655-660 (2018). https://doi.org/10.1038/s41586-018-0444-0

82 Xin, Q. *et al.* Polycomb subunit BMI1 determines uterine progesterone responsiveness essential for normal embryo implantation. *J Clin Invest* **128**, 175-189 (2018). https://doi.org/10.1172/JCI92862

83 Tang, Y. *et al.* P38alpha MAPK is a gatekeeper of uterine progesterone responsiveness at peri-implantation via Ube3c-mediated PGR degradation. *Proc Natl Acad Sci U S A* **119**, e2206000119 (2022). https://doi.org/10.1073/pnas.2206000119

84 Lessey, B. A. & Young, S. L. Homeostasis imbalance in the endometrium of women with implantation defects: the

role of estrogen and progesterone. *Semin Reprod Med* **32**, 365-375 (2014). https://doi.org/10.1055/s-0034-1376355

85 Young, S. L. Oestrogen and progesterone action on endometrium: a translational approach to understanding endometrial receptivity. *Reprod Biomed Online* **27**, 497-505 (2013). https://doi.org/10.1016/j.rbmo.2013.06.010

86 Usoskin, D. *et al.* Unbiased classification of sensory neuron types by large-scale single-cell RNA sequencing. *Nat Neurosci* **18**, 145-153 (2015). https://doi.org/10.1038/nn.3881

87 Bahrami, S. & Drablos, F. Gene regulation in the immediate-early response process. *Adv Biol Regul* **62**, 37-49 (2016). https://doi.org/10.1016/j.jbior.2016.05.001

88 Coughlan, C. *et al.* Recurrent implantation failure: definition and management. *Reprod Biomed Online* **28**, 14-38 (2014). https://doi.org/10.1016/j.rbmo.2013.08.011

89 Verbitsky, A., Dopfel, D. & Zhang, N. Rodent models of post-traumatic stress disorder: behavioral assessment. *Transl Psychiatry* **10**, 132 (2020). https://doi.org/10.1038/s41398-020-0806-x

90 Kastan, N. R. *et al.* Development of an improved inhibitor of Lats kinases to promote regeneration of mammalian organs. *Proc Natl Acad Sci U S A* **119**, e2206113119 (2022). https://doi.org/10.1073/pnas.2206113119

91 Sountoulidis, A. *et al.* SCRINSHOT enables spatial mapping of cell states in tissue sections with single-cell resolution. *PLoS Biol* **18**, e3000675 (2020). https://doi.org/10.1371/journal.pbio.3000675

Acknowledgments

The authors thank Prof. Wen-Bo Deng for kindly providing *PGR-A* and *PGR-B* plasmids. We thank Prof. Gui-Jun Yan from Nanjing University and Dr. Chen Chen for their valuable suggestion that inspire this study. We thank Hanhui Hong from Accuramed Biotech Co., Ltd. (Guangzhou, China) for assistance with single-cell transcriptomics bioinformatics analysis. We also thank our colleagues at the Laboratory Animal Center of South China Agricultural University for their excellent support in maintaining all the animals used in this study. At last, we thank LetPub (www.letpub.com.cn) for linguistic assistance and pre-submission expert review.

Funding

National Natural Science Foundation of China Nos. 32471173 and 31771664

GuangDong Basic and Applied Basic Research Foundation No. 2025A1515140093

Funding from Key Laboratory of Assisted Reproduction (Peking University), Ministry of Education No. BYSYSZKF2026008

Specific University Discipline Construction Project No. 2023B10564003.

Author contributions

Conceptualization: JWK, ZMY, BG, HLD, RWS

Methodology: JWK, YZ, BG, RWS

Investigation: JWK, YZ, HXL, HZ, JYY, XQH, JYY, RZ, YNL

Resources: ZWA, YZ

Funding acquisition: RWS

Supervision: ZMY, BG, HLD, RWS

Writing – original draft: JWK, RWS

Writing – review and editing: JWK, YZ, ZMY, BG, HLD, RWS

Competing interests

The authors declare that they have no competing interests.

Data availability

The single-cell RNA sequencing data generated in this study have been deposited in the Gene Expression

Omnibus (GEO) database under accession number GSE285982. All other data supporting the findings of this study are available in the main text, the supplementary materials, and can be obtained from the corresponding authors upon reasonable request. Mouse lines generated in this study are available from the corresponding author upon reasonable request and subject to a materials transfer agreement (MTA).

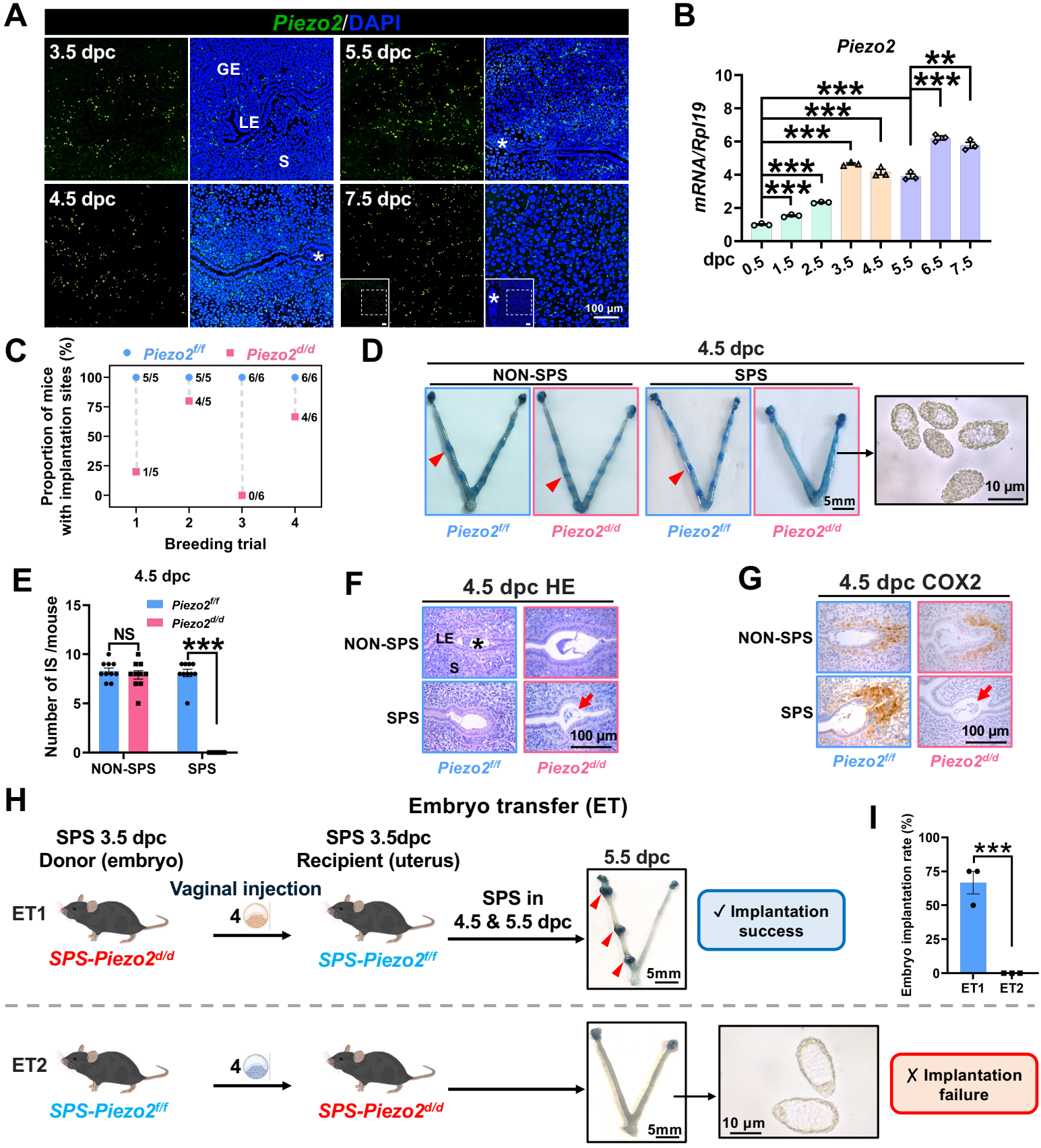
A
Piezo2/DAPI
3.5 dpc
GE
LE
S
5.5 dpc
4.5 dpc
7.5 dpc
100 μm
B
Piezo2
mRNA/Rpl19
dpc
0.5
1.5
2.5
3.5
4.5
5.5
6.5
7.5
C
Piezo2f/f
Piezo2d/d
Proportion of mice with implantation sites (%)
Breeding trial
5/5
4/5
6/6
4/6
1/5
0/6
D
4.5 dpc
NON-SPS
SPS
5mm
10 μm
E
4.5 dpc
Number of IS /mouse
NS
***
NON-SPS
SPS
F
4.5 dpc HE
NON-SPS
SPS
LE
S
100 μm
G
4.5 dpc COX2
NON-SPS
SPS
100 μm
H
Embryo transfer (ET)
SPS 3.5 dpc
Donor (embryo)
SPS 3.5dpc
Recipient (uterus)
Vaginal injection
ET1
SPS-Piezo2d/d
SPS-Piezo2f/f
SPS in
4.5 & 5.5 dpc
5.5 dpc
5mm
✓ Implantation success
ET2
SPS-Piezo2f/f
SPS-Piezo2d/d
5mm
10 μm
✗ Implantation failure
I
Embryo implantation rate (%)
ET1
ET2

Fig. 1. Maternal stress impairs embryo implantation in a PIEZO2-dependent manner. (**A**) Single-molecule fluorescence *in situ* hybridization (smFISH) of *Piezo2* mRNA (green) and DAPI nuclear staining (blue) in mouse uterine cross-sections at 3.5, 4.5, 5.5, and 7.5 dpc. *Piezo2* transcripts are predominantly localized in endometrial stromal cells. Asterisks indicate embryos. Dashed boxes indicate magnified regions shown in insects. GE, glandular epithelium; LE, luminal epithelium; S, stroma. Scale bar, 100 μm. (**B**) Quantitative RT-PCR analysis of *Piezo2* mRNA expression in the mouse uterus across the peri-implantation period (0.5-7.5 dpc). *Piezo2* expression was progressively upregulated from 3.5 dpc onward, coinciding with the window of implantation and decidualization. Expression was normalized to *Rpl19* and based on $n = 3$ biologically independent samples per timepoint (two-sided Student's *t*-test). **(C**) Implantation rates of $Piezo2^{f/f}$ (pink) and $Piezo2^{d/d}$ (blue) females at 4.5 dpc across four independent breeding trials. Each data point represents the proportion of mice with implantation sites in a given trial. Fractions indicate the number of mice with implantation sites out of total mice examined. Control mice consistently achieved 100% implantation, while $Piezo2^{d/d}$ mice showed highly variable implantation rates (0-80%). (**D**) Representative $Piezo2^{d/d}$ and $Piezo2^{f/f}$ uterine images at 4.5 dpc with or without modified Single Prolonged Stress (SPS) treatment. Implantation sites were visualized by intravenous injection of Chicago Sky Blue dye (blue spots) and indicated with red arrowheads. SPS completely abolished implantation in $Piezo2^{d/d}$ mice while having no effect on the controls. Right panel: morphologically normal blastocysts recovered from the uterine lumen of SPS-$Piezo2^{d/d}$. Scale bars, 5 mm (uteri) and 10 μm (blastocysts). (**E**) Quantification of implantation site number per mouse in $Piezo2^{d/d}$ and $Piezo2^{f/f}$ females with or without SPS treatment at 4.5 dpc. Each dot represents one mouse ($n = 10$ per group, two-way ANOVA with Tukey's post hoc test). **(F**) Histological analysis (H&E staining) of uterine cross-sections at 4.5 dpc from $Piezo2^{d/d}$ and $Piezo2^{f/f}$ mice with or without SPS treatment. Asterisks indicate embryos within the uterine lumen and the red arrows indicate unattached embryos. S, stroma; LE, luminal epithelium. Scale bar, 100 μm. (**G**) Immunohistochemistry detecting COX2 in uterine sections at 4.5 dpc. COX2, a marker of endometrial receptivity and decidualization, was strongly expressed at implantation sites in *Piezo2* controls regardless of SPS treatment but absent in SPS-$Piezo2^{d/d}$ uteri (red arrow). Scale bar, 100 μm. (**H**) Schematic of the reciprocal embryo transfer (ET) strategy. Blastocysts (3.5 dpc) from SPS-treated donors were transferred via vaginal injection (4 embryos per recipient) into pseudopregnant SPS-treated recipients of the reciprocal genotype, and implantation was assessed on 5.5 dpc. Representative uterine images are shown. ET1: $Piezo2^{d/d}$ embryos to $Piezo2^{f/f}$ uteri = implantation success (red arrowheads). ET2: $Piezo2^{f/f}$ embryos to $Piezo2^{d/d}$ uteri = implantation failure; morphologically normal

blastocysts recovered from the uterine lumen. Scale bars, 5 mm (uteri) and 10 μm (blastocysts). (**I**) Quantification of embryo implantation rate following reciprocal embryo transfer. Each dot represents one recipient mouse (two-sided Student's *t*-test). Quantitative data are presented as mean ± SEM. ns, $P > 0.05$; $^{**}P < 0.01$; $^{***}P < 0.001$.

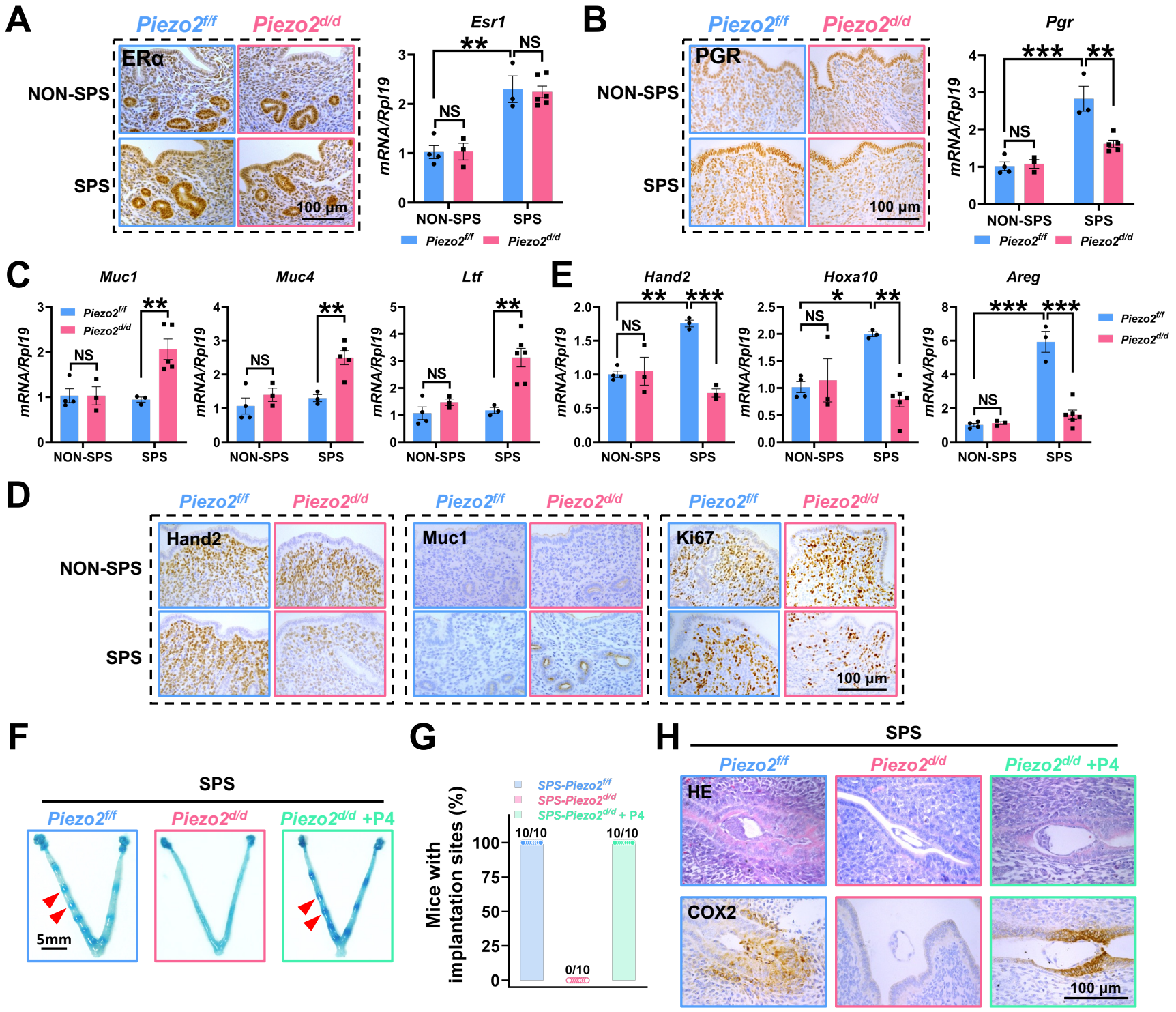
A
Piezo2f/f
Piezo2d/d
ERα
NON-SPS
SPS
100 μm
Esr1
mRNA/Rpl19
NS
**
NS
NON-SPS
SPS
Piezo2f/f
Piezo2d/d
B
PGR
Pgr
***
**
C
Muc1
Muc4
Ltf
E
Hand2
Hoxa10
Areg
D
Ki67
F
SPS
5mm
G
Mice with implantation sites (%)
SPS-Piezo2f/f
SPS-Piezo2d/d
SPS-Piezo2d/d + P4
10/10
0/10
H
HE
COX2

Fig. 2. PIEZO2 preserves uterine receptivity by maintaining progesterone signaling under stress. **(A)** Immunohistochemistry (left) and quantitative RT-PCR (right) for ERα (ESR1) in uterine sections at 3.5 dpc from *Piezo2*$^{d/d}$ and *Piezo2*$^{f/f}$ mice with or without SPS treatment. SPS increased ESR1 expression in the endometrium of both genotypes to comparable levels (n > 3 per group, two-way ANOVA with Tukey's post hoc test). Scale bar, 100 μm. (**B**) Immunohistochemistry (left) and quantitative RT-PCR (right) for PGR in uterine sections at 3.5 dpc. PGR expression was robustly induced by SPS in *Piezo2*$^{f/f}$ mice but failed to increase in *Piezo2*$^{d/d}$ mice (n > 3 per group, two-way ANOVA with Tukey's post hoc test). Scale bar, 100 μm. **(C and E**) Quantitative RT-PCR analysis of estrogen-responsive genes (*Muc1*, *Muc4*, *Ltf*) (**C**) and progesterone-responsive genes (*Hand2*, *Hoxa10*, *Areg*) (**E**) in SPS-treated and untreated *Piezo2*$^{d/d}$ and control uteri at 3.5 dpc. Expression was normalized to *Rpl19* (n = 3 per group, two-way ANOVA with Tukey's post hoc test). (**D**) Immunohistochemistry detecting Hand2 (progesterone-responsive), Muc1 (estrogen-responsive), and Ki67 (proliferation marker) in uterine sections at 3.5 dpc from *Piezo2*$^{f/f}$ and *Piezo2*$^{d/d}$ mice with or without SPS treatment. Scale bar, 100 μm. (**F and G**) Representative uterine images at 4.5 dpc from SPS-*Piezo2*$^{f/f}$, SPS-*Piezo2*$^{d/d}$, and SPS-*Piezo2*$^{d/d}$+P4 (progesterone-supplemented) mice. Implantation sites were visualized by intravenous injection of Chicago Sky Blue dye (blue spots) and indicated with red arrowheads, with the results per group graphically displayed (n = 10 per group). Scale bar, 5 mm. (**H**) Histological analysis (H&E staining, top) and immunohistochemistry for COX2 (bottom) in uterine sections at 4.5 dpc from SPS-*Piezo2*$^{f/f}$, SPS-*Piezo2*$^{d/d}$, and SPS-*Piezo2*$^{d/d}$+P4 mice. Progesterone (P4) restored decidual morphology and COX2 expression in SPS-*Piezo2*$^{d/d}$ uteri. Scale bar, 100 μm. Quantified data are presented as mean ± SEM. ns, $P > 0.05$; $^{**}P < 0.01$; $^{***}P < 0.001$.

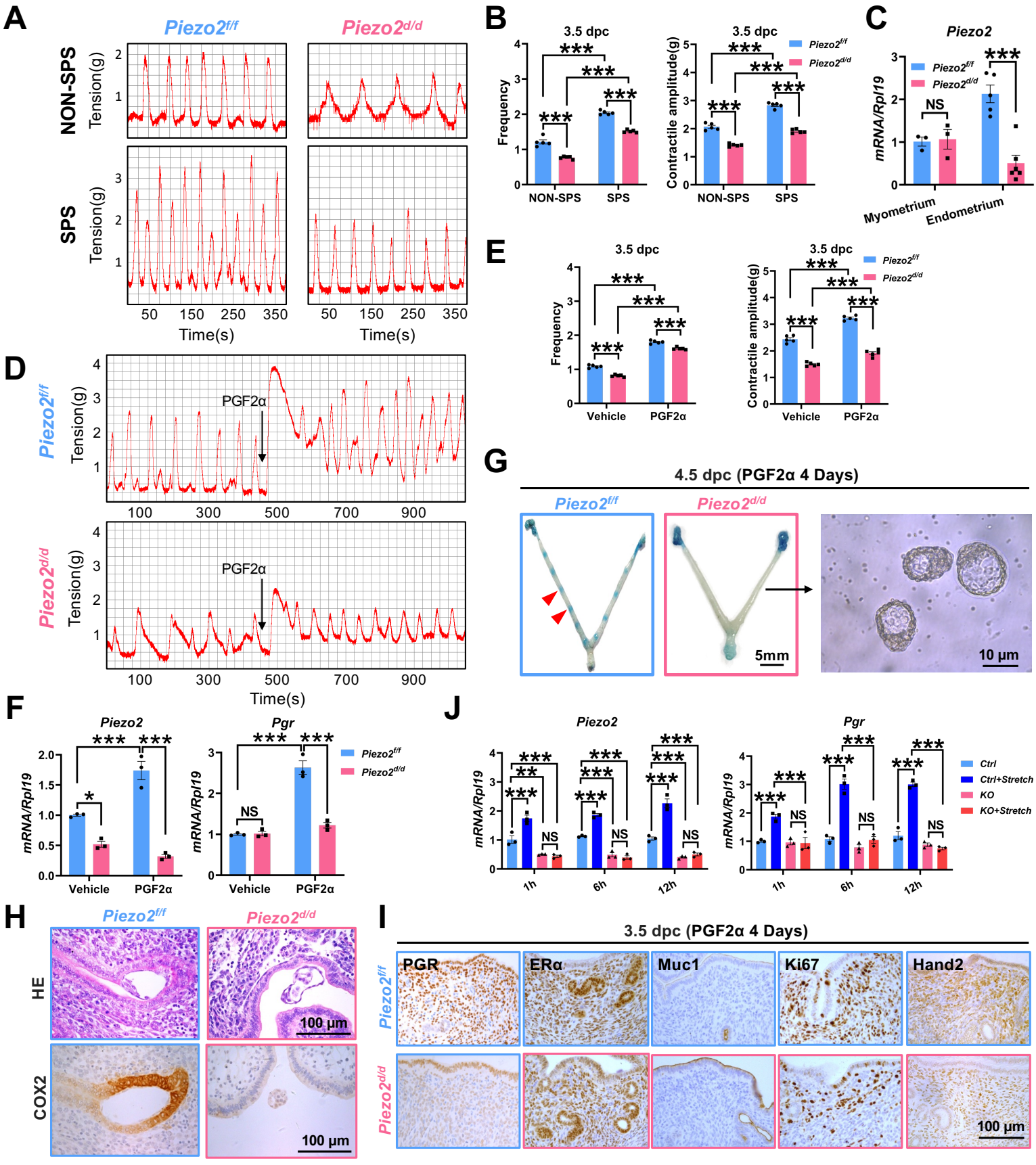
A
Piezo2f/f
Piezo2d/d
NON-SPS
SPS
Tension(g)
Time(s)
B
3.5 dpc
Frequency
Contractile amplitude(g)
NON-SPS
SPS
C
Piezo2
mRNA/Rpl19
NS
Myometrium
Endometrium
D
PGF2α
Tension(g)
Time(s)
E
3.5 dpc
Frequency
Contractile amplitude
Vehicle
PGF2α
F
Piezo2
Pgr
mRNA/Rpl19
Vehicle
PGF2α
G
4.5 dpc (PGF2α 4 Days)
5mm
10 μm
H
HE
COX2
100 μm
I
3.5 dpc (PGF2α 4 Days)
PGR
ERα
Muc1
Ki67
Hand2
100 μm
J
Piezo2
Pgr
mRNA/Rpl19
Ctrl
Ctrl+Stretch
KO
KO+Stretch
1h
6h
12h

Fig. 3. Stress-induced uterine contractions activate PIEZO2 mechanosensing. (**A and B**) Representative *ex vivo* tension traces from *Piezo2*$^{d/d}$ and *Piezo2*$^{f/f}$ uteri with or without SPS treatment (**A**), and quantification of contraction frequency (left) and contractile amplitude (right) based on recordings (**B**) (n = 5 per group). (**C**) Quantitative RT-PCR analysis of *Piezo2* expression in surgically isolated endometrial and myometrial layers. *Piezo2* expression was normalized to *Rpl19* (n > 3 per group). (**D and E**) Representative *ex vivo* tension traces from *Piezo2*$^{d/d}$ (bottom) and *Piezo2*$^{f/f}$ (top) uteri treated with prostaglandin F2α (PGF2α) (**D**), and quantification of contraction frequency (left) and amplitude (right) following PGF2α treatment (**E**) (n = 5 per group). (**F**) Quantitative RT-PCR analysis of *Piezo2* and *Pgr* expression in *Piezo2*$^{f/f}$ and *Piezo2*$^{d/d}$ uteri following *ex vivo* PGF2α treatment. *Piezo2* and *Pgr* expression were normalized to *Rpl19* (n = 3 per group). (**G**) Representative uterine images at 4.5 dpc following *in vivo* PGF2α administration during the peri-implantation period. Implantation sites were visualized by intravenous injection of Chicago Sky Blue dye (blue spots) and indicated with red arrowheads. Morphologically normal blastocysts were recovered from the *Piezo2*$^{d/d}$ uterine lumen (right). Scale bars, 5 mm and 100 μm. (**H**) Histological analysis (H&E staining) and immunohistochemistry detecting COX2 in uterine sections at 4.5 dpc following PGF2α treatment. Scale bar, 100 μm. (**I**) Immunohistochemistry for PGR, ERα, Muc1, Ki67, and Hand2 in uterine sections at 3.5 dpc from PGF2α-treated *Piezo2*$^{f/f}$ and *Piezo2*$^{d/d}$ mice. *Piezo2*$^{d/d}$ shows upregulated Muc1 and ERα, and downregulated PGR, Hand2, and Ki67. Scale bar, 100 μm. (**J**) Quantitative RT-PCR analysis of *Piezo2* and *Pgr* expression following direct mechanical stretching of isolated uteri *ex vivo*. *Piezo2* and *Pgr* expression were quantified at 1, 6, and 12 h and normalized to *Rpl19* (n = 3 per group). Quantitative data are presented as mean ± SEM. Statistical significance was determined by using a two-way ANOVA with Tukey's post hoc test. ns, $P > 0.05$; $^{**}P < 0.01$; $^{***}P < 0.001$.

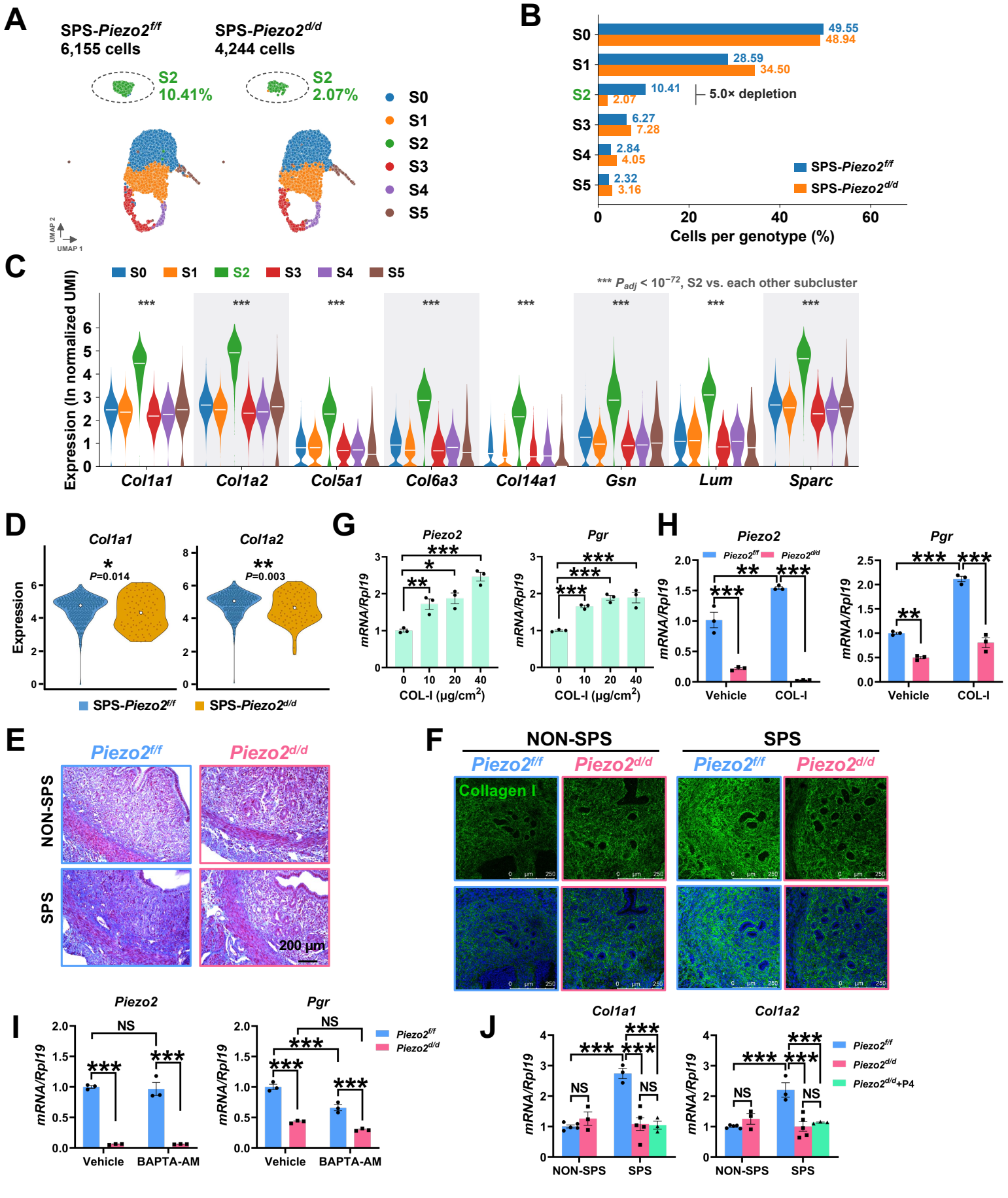
A
SPS-Piezo2f/f
6,155 cells
SPS-Piezo2d/d
4,244 cells
S2
10.41%
S2
2.07%
S0
S1
S2
S3
S4
S5
UMAP 2
UMAP 1
B
S0
S1
S2
S3
S4
S5
49.55
48.94
28.59
34.50
10.41
2.07
5.0× depletion
6.27
7.28
2.84
4.05
2.32
3.16
SPS-Piezo2f/f
SPS-Piezo2d/d
0
20
40
60
Cells per genotype (%)
C
S0
S1
S2
S3
S4
S5
*** Padj < 10−72, S2 vs. each other subcluster
Expression (ln normalized UMI)
Col1a1
Col1a2
Col5a1
Col6a3
Col14a1
Gsn
Lum
Sparc
D
Col1a1
Col1a2
Expression
*
P=0.014
**
P=0.003
SPS-Piezo2f/f
SPS-Piezo2d/d
G
Piezo2
Pgr
mRNA/Rpl19
COL-I (μg/cm2)
H
Piezo2
Pgr
Piezo2f/f
Piezo2d/d
mRNA/Rpl19
Vehicle
COL-I
E
Piezo2f/f
Piezo2d/d
NON-SPS
SPS
200 μm
F
NON-SPS
SPS
Piezo2f/f
Piezo2d/d
Collagen I
I
Piezo2
Pgr
mRNA/Rpl19
NS
Vehicle
BAPTA-AM
Piezo2f/f
Piezo2d/d
J
Col1a1
Col1a2
mRNA/Rpl19
NS
NON-SPS
SPS
Piezo2f/f
Piezo2d/d
Piezo2d/d+P4

Fig. 4. PIEZO2 promotes endometrial extracellular matrix remodeling to support progesterone signaling. (**A**) UMAP visualization of mesenchymal fibroblast subclusters identified by scRNA-seq in SPS-*Piezo2*$^{d/d}$ and SPS-*Piezo2*$^{f/f}$ uteri at 3.5 dpc. Each point represents a single fibroblast and is colored according to its assigned subcluster (S0-S5). Dashed ellipses demarcate the ECM-high S2 island, whose share of the fibroblast compartment falls from 10.41% to 2.07% upon Piezo2 deletion. (**B**) Fractional composition of the fibroblast compartment by subcluster, expressed as a percentage of all fibroblasts recovered from that genotype (percentages given to the right of each bar). S2 is the only subcluster showing selective depletion (5.0-fold); the remaining subclusters vary by <1.3-fold. Blue, SPS-*Piezo2*$^{f/f}$; orange, SPS-*Piezo2*$^{d/d}$. (**C**) Violin plots showing the expression of fibroblast/stromal extracellular matrix (ECM)-associated genes (*Col1a1*, *Col1a2*, *Col13a1*, *Col5a1*, *Col6a3*, *Col14a1*, *Gsn*, *Lum*, and *Sparc*) across the identified cell subclusters (0-5) from uterine single-cell RNA-sequencing. White bars denote medians and colors denote subcluster identity as in (A). S2 expresses every gene at higher levels than each of the five other subclusters individually (***, all 40 pairwise comparisons $P_{adj} < 10^{-72}$, two-sided Mann-Whitney U test with Benjamini-Hochberg correction; AUROC 0.87-0.97). Alternating shading separates adjacent genes. (**D**) Violin plots comparing the expression of *Col1a1* and *Col1a2* between SPS-*Piezo2*$^{f/f}$ and SPS-*Piezo2*$^{d/d}$ uteri. $P = 0.014$ for *Col1a1* and $P = 0.003$ for *Col1a2*. *P < 0.05, **P < 0.01. (**E**) Representative Masson's trichrome staining of uterine sections at 3.5 dpc. Blue staining indicates collagen deposition, muscle/cytoplasm is red, and the nuclei are dark blue/black. Scale bar, 200 μm. (**F**) Representative immunofluorescence detecting type I collagen (COL-I) in uterine sections at 3.5 dpc from non-SPS and SPS-treated *Piezo2*$^{d/d}$ and *Piezo2*$^{f/f}$. COL-I deposition in the endometrium alone (top, green) and merged with DAPI (bottom, blue). Scale bar, 250 μm. (**G**) Quantitative RT-PCR analysis of *Piezo2* and *Pgr* expression in primary uterine stromal cells cultured on increasing densities of COL-I. Cells were cultured for 48h at various COL-I coating densities prior to RNA extraction to evaluate the density-dependent response induced by collagen. Expression was normalized to *Rpl19* ($n = 3$ per group, two-sided Student's *t*-test). (**H**) Quantitative RT-PCR analysis of *Piezo2* and *Pgr* expression in *Piezo2*$^{d/d}$ and *Piezo2*$^{f/f}$ cells cultured on COL-I (10 μg/cm^2). RNA was extracted after culturing for 48h, and mRNA expression was normalized to *Rpl19* ($n = 3$ per group, two-way ANOVA with Tukey's post hoc test). (**I**) Effect of Ca^{2+} chelation (BAPTA-AM, 10 μM) on collagen-induced *Piezo2* and *Pgr* expression in *Piezo2*$^{d/d}$ and *Piezo2*$^{f/f}$ cells. Plates were coated with COL-I (10 μg/cm^2) and cells were cultured with BAPTA-AM or Vehicle for 48h prior to RNA extraction. Expression was normalized to *Rpl19* ($n = 3$ per group, two-way ANOVA with Tukey's post hoc test). (**J**) Quantitative RT-PCR analysis of collagen gene expression

(*Col1a1*, *Col1a2*) in *Piezo2*$^{f/f}$, *Piezo2*$^{d/d}$, SPS-*Piezo2*$^{f/f}$, SPS-*Piezo2*$^{d/d}$, and SPS-*Piezo2*$^{d/d}$+P4 uteri. Expression normalized to *Rpl19* (n = 3 per group, two-way ANOVA with Tukey's post hoc test). Quantified data are presented as mean ± SEM. ns, $P > 0.05$; *$P < 0.05$; **$P < 0.01$; ***$P < 0.001$.

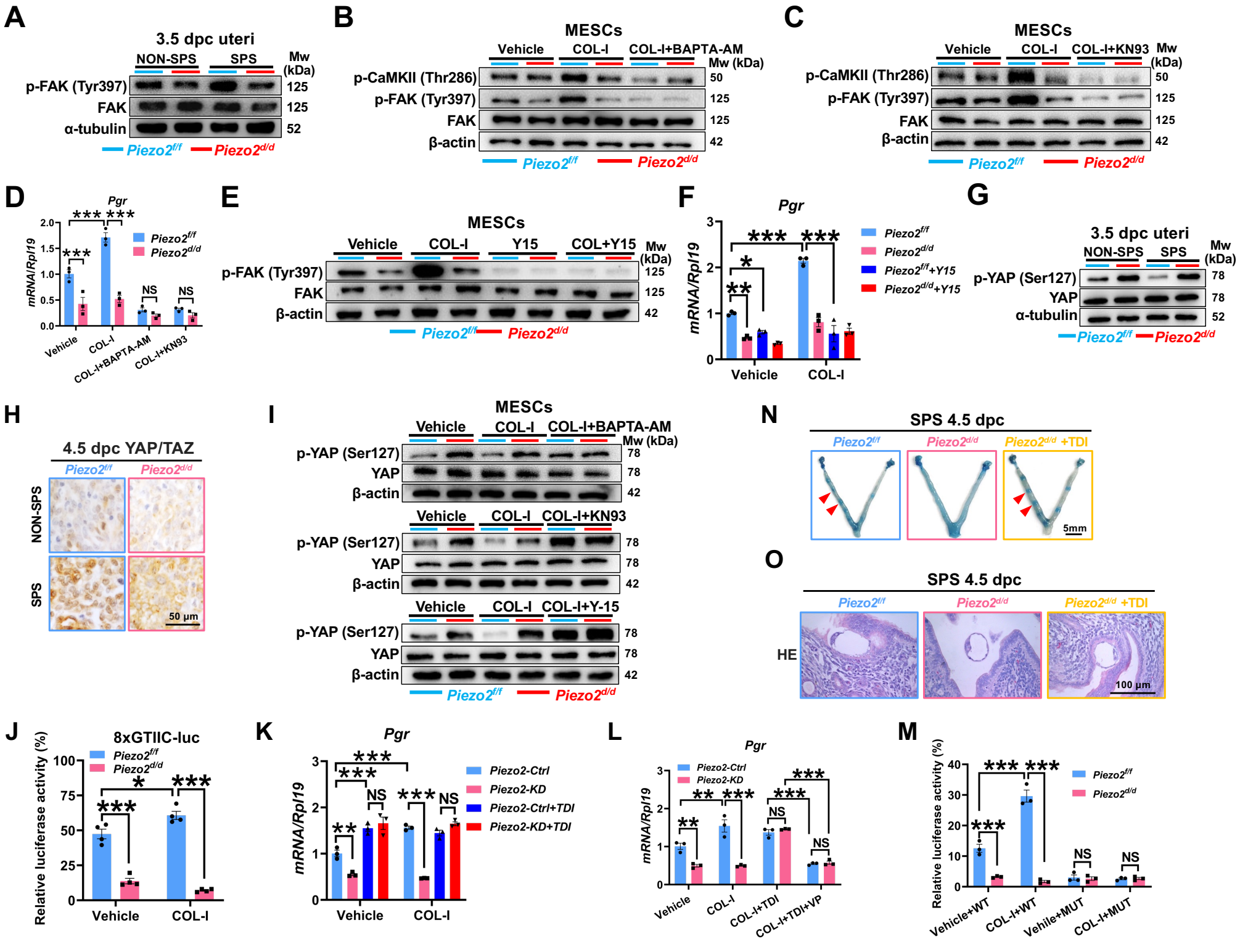
A
3.5 dpc uteri
NON-SPS
SPS
Mw (kDa)
p-FAK (Tyr397)
FAK
α-tubulin
125
125
52
Piezo2f/f
Piezo2d/d
B
MESCs
Vehicle
COL-I
COL-I+BAPTA-AM
Mw (kDa)
p-CaMKII (Thr286)
p-FAK (Tyr397)
FAK
β-actin
50
125
125
42
C
MESCs
Vehicle
COL-I
COL-I+KN93
p-CaMKII (Thr286)
p-FAK (Tyr397)
FAK
β-actin
D
Pgr
mRNA/Rpl19
NS
Vehicle
COL-I
COL-I+BAPTA-AM
COL-I+KN93
E
MESCs
Vehicle
COL-I
Y15
COL+Y15
p-FAK (Tyr397)
FAK
β-actin
F
Pgr
mRNA/Rpl19
Piezo2f/f+Y15
Piezo2d/d+Y15
G
3.5 dpc uteri
p-YAP (Ser127)
YAP
α-tubulin
H
4.5 dpc YAP/TAZ
NON-SPS
SPS
50 μm
I
MESCs
COL-I+Y-15
p-YAP (Ser127)
YAP
β-actin
N
SPS 4.5 dpc
Piezo2d/d +TDI
5mm
O
HE
100 μm
J
8xGTIIC-luc
Relative luciferase activity (%)
K
Pgr
mRNA/Rpl19
Piezo2-Ctrl
Piezo2-KD
Piezo2-Ctrl+TDI
Piezo2-KD+TDI
L
Pgr
COL-I+TDI
COL-I+TDI+VP
M
Relative luciferase activity (%)
Vehicle+WT
COL-I+WT
Vehile+MUT
COL-I+MUT

Fig. 5. PIEZO2-collagen signaling activates FAK-Hippo-YAP pathway to drive progesterone receptor transcription. (**A**) Western blot analysis of phosphorylated FAK (p-FAK, Tyr397) and total FAK in uterine tissues at 3.5 dpc from *Piezo2*$^{d/d}$ and *Piezo2*$^{f/f}$ mice with or without SPS treatment. Relative expression was determined by normalizing to α-tubulin and based on $n = 3$ per group (graph in Extended data Fig. 6A). (**B**) Western blot analysis of p-CaMKII (Thr286), p-FAK (Tyr397), and total FAK in primary MESCs from *Piezo2*$^{f/f}$ and *Piezo2*$^{d/d}$ mice. Samples were culture without COL-I or treatment (Vehicle), with COL-I coating, or with COL-I coating and BAPTA-AM (10 μM, Ca^{2+} chelator). At 48h post-treatment, cells were lysed and relative expression was determined by normalizing to β-actin ($n = 3$ per group, graph in Extended data Fig. 6B). (**C**) Western blot analysis of p-CaMKII, p-FAK, and total FAK in MESCs from *Piezo2*$^{f/f}$ and *Piezo2*$^{d/d}$ mice cultured on COL-I with or without KN93 (10 μM, CaMKII inhibitor). Samples were cultured without COL-I or treatment (Vehicle), with COL-I coating, or with COL-I coating and CaMKII inhibitor. At 48h post-treatment, cells were lysed and relative expression was determined by normalizing to β-actin ($n = 3$ per group, graph in Extended data Fig. 6C). (**D**) Quantitative RT-PCR analysis of *Pgr* expression in *Piezo2*$^{f/f}$ and *Piezo2*$^{d/d}$ MESCs cultured on COL-I with or without BAPTA-AM or KN93. Cells were cultured on COL-I coated plates, with the control cultured without COL-I or treatment (Vehicle), and RNA was extracted at 48h post-treatment. Expression was normalized to *Rpl19* ($n = 3$ per group). (**E**) Western blot analysis of p-FAK (Tyr397) and total FAK in MESCs from *Piezo2*$^{f/f}$ and *Piezo2*$^{d/d}$ mice treated with Y15 (FAK inhibitor). Cells were cultured with COL-I coating, Y15 (10 μM, no COL-I), or COL-I+Y15, with a control cultured without COL-I coating or treatment (Vehicle). Cultures were maintained for 48 h and then lysed. Relative expression was determined by normalizing to β-actin and based on $n = 3$ independent experiments, graph in Extended data Fig. 6D. (**F**) Quantitative RT-PCR analysis of *Pgr* expression in *Piezo2*$^{f/f}$ and *Piezo2*$^{d/d}$ MESCs treated with or without Y15 in the presence of COL-I. Cells were cultured with COL-I or without (vehicle) and with or without Y15 for 48h prior to RNA extraction. Expression was normalized to *Rpl19* ($n = 3$ per group). (**G**) Western blot analysis of p-YAP (Ser127) and total YAP in uterine tissues at 3.5 dpc from *Piezo2*$^{f/f}$ and *Piezo2*$^{d/d}$ mice with or without SPS treatment. Expression was normalized to α-tubulin ($n = 3$ per group, graphs in Extended data Fig. 6F). (**H**) Immunohistochemistry detecting YAP/TAZ in uterine sections at 4.5 dpc from *Piezo2*$^{f/f}$ and *Piezo2*$^{d/d}$ mice with or without SPS treatment. SPS promoted nuclear YAP localization (brown staining in stromal nuclei) in *Piezo2*$^{f/f}$ but not in *Piezo2*$^{d/d}$ endometrial stroma. Scale bar, 50 μm. (**I**) Western blot analysis of p-YAP (Ser127) and total YAP in *Piezo2*$^{f/f}$ and *Piezo2*$^{d/d}$ MESCs cultured on COL-I with BAPTA-AM, KN93, or Y15 treatment. Cells were cultured with COL-I

or without (Vehicle) and with or without treatment for 48h prior to RNA extraction. Expression was normalized to *Rpl19* (n = 3 per group, quantification is shown in Extended data Fig. 6G). (**J**) TEAD reporter assay in *Piezo2*$^{d/d}$ and control MESCs. Cells were co-transfected with 8×GTIIC luciferase reporter plasmid (1 μg) and pRL-SV40 *Renilla* luciferase (100 ng), cultured for 48 h and lysed. Firefly luciferase values were normalized to *Renilla* luciferase (n = 3 independent experiments). (**K**) Quantitative RT-PCR analysis of *Pgr* expression in *Piezo2*$^{f/f}$ and *Piezo2*$^{d/d}$ MESCs treated with LATS1/2 inhibitor. Cells were cultured on plates coated with COL-I or without Col-I (vehicle) and with or without TDI-011536 (3 μM; TDI, LATS1/2 inhibitor). RNA was extracted at 48h post-treatment and expression was normalized to *Rpl19* (n = 3 per group). (**L**) Quantitative RT-PCR analysis of *Pgr* expression in MESCs treated with TDI (LATS1/2 inhibitor) or verteporfin (VP, YAP-TEAD inhibitor) in the presence of COL-I. Controls were cultured on plates coated with COL-I or without Col-I or treatment (Vehicle). RNA was extracted at 48h post-treatment and expression was normalized to *Rpl19* (n = 3 per group). (**M)** Luciferase reporter assay examining the TEAD-binding site within the *Pgr* promoter in cultured MESCs. Cells were co-transfected with either pGL3-*Pgr* (wild-type) or pGL3-*Pgr*-mutant (mutant) and a pRL-SV40 plasmid. Cells were cultured for 48 h and lysed. Firefly luciferase values were normalized to *Renilla* luciferase (n = 3 independent experiments). (**N and O**) Pharmacological inhibition of Hippo signaling with TDI rescues implantation in SPS-*Piezo2*-cKO mice at 4.5 dpc. Red arrowheads indicate implantation sites visualized by Chicago Sky Blue dye injection (**N**). Histological analysis (H&E staining) confirming restored decidualization in TDI-treated SPS-*Piezo2*$^{d/d}$ uteri (**O**). Scale bars, 5 mm and 100 μm. Quantitative data are presented as mean ± SEM. Statistical significance was determined using a two-way ANOVA with Tukey's post hoc test. ns, $P > 0.05$; *$P < 0.05$; **$P < 0.01$; ***$P < 0.001$.

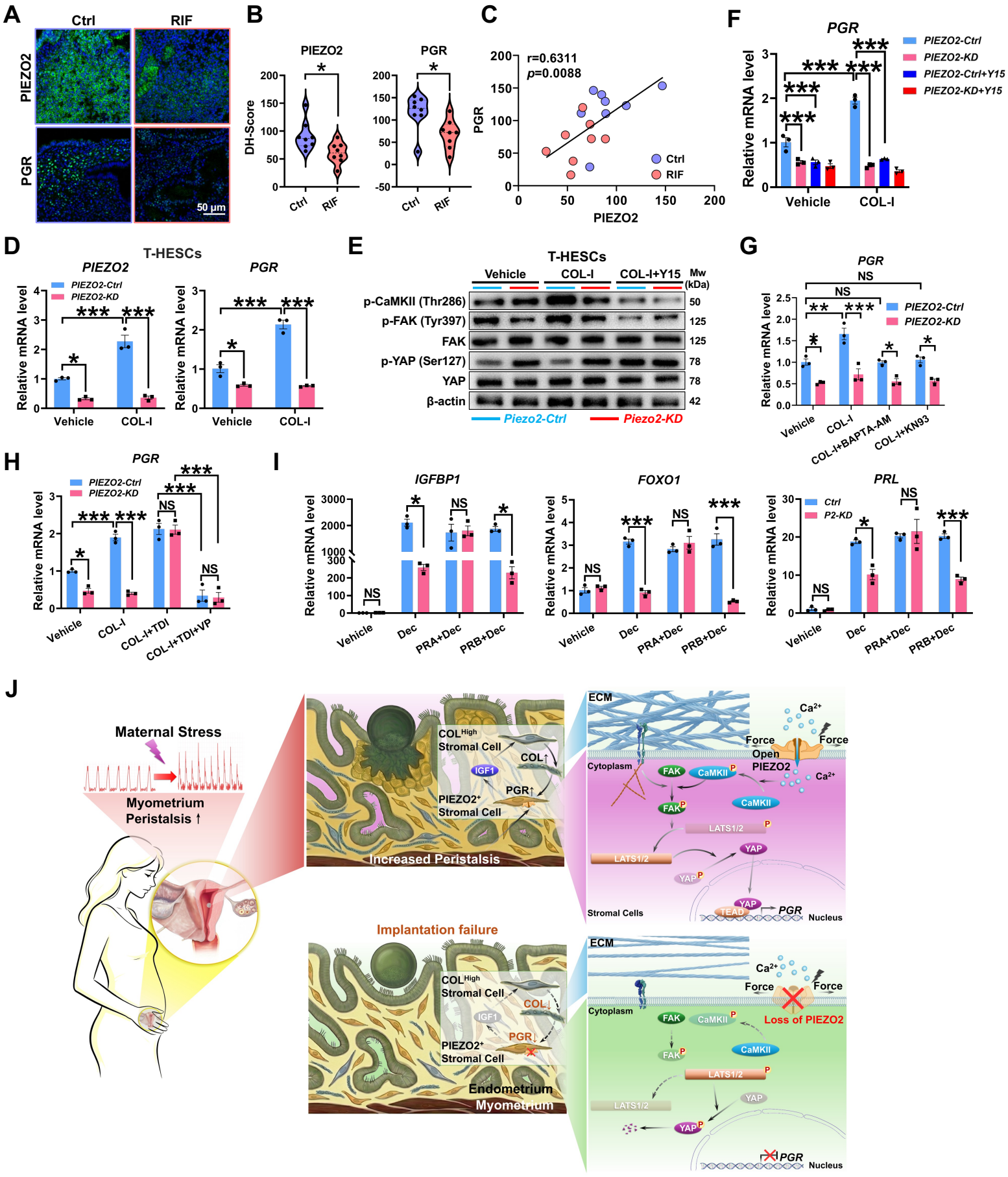
A
Ctrl
RIF
PIEZO2
PGR
50 μm
B
PIEZO2
PGR
DH-Score
Ctrl
RIF
C
r=0.6311
p=0.0088
PGR
PIEZO2
Ctrl
RIF
F
PGR
PIEZO2-Ctrl
PIEZO2-KD
PIEZO2-Ctrl+Y15
PIEZO2-KD+Y15
Relative mRNA level
Vehicle
COL-I
D
T-HESCs
PIEZO2
PGR
PIEZO2-Ctrl
PIEZO2-KD
Relative mRNA level
Vehicle
COL-I
E
T-HESCs
Vehicle
COL-I
COL-I+Y15
Mw (kDa)
p-CaMKII (Thr286)
p-FAK (Tyr397)
FAK
p-YAP (Ser127)
YAP
β-actin
Piezo2-Ctrl
Piezo2-KD
G
PGR
NS
PIEZO2-Ctrl
PIEZO2-KD
Relative mRNA level
Vehicle
COL-I
COL-I+BAPTA-AM
COL-I+KN93
H
PGR
PIEZO2-Ctrl
PIEZO2-KD
Relative mRNA level
Vehicle
COL-I
COL-I+TDI
COL-I+TDI+VP
I
IGFBP1
FOXO1
PRL
Ctrl
P2-KD
Relative mRNA level
Vehicle
Dec
PRA+Dec
PRB+Dec
J
Maternal Stress
Myometrium Peristalsis ↑
COL^High Stromal Cell
COL↑
IGF1
PGR↑
PIEZO2+ Stromal Cell
Increased Peristalsis
ECM
Ca2+
Force
Force
Open PIEZO2
Cytoplasm
FAK
CaMKII
P
Ca2+
FAK
CaMKII
LATS1/2
YAP
LATS1/2
YAP
Stromal Cells
YAP
TEAD
PGR
Nucleus
Implantation failure
COL^High Stromal Cell
COL↓
IGF1
PGR↓
PIEZO2+ Stromal Cell
Endometrium
Myometrium
ECM
Ca2+
Force
Force
Cytoplasm
FAK
CaMKII
Loss of PIEZO2
FAK
CaMKII
LATS1/2
YAP
LATS1/2
YAP
PGR
Nucleus

Fig. 6. The PIEZO2-collagen-PGR cascade is conserved in humans and contributes to recurrent implantation failure (RIF). (**A**) Representative immunofluorescent images detecting PIEZO2 (green, top) and PGR (green, bottom) with DAPI counterstaining (blue) in endometrial biopsies from fertile controls (Ctrl, $n = 8$) and patients with recurrent implantation failure (RIF, $n = 8$). Both PIEZO2 and PGR were significantly reduced in endometrial stroma from RIF patients. Scale bar, 50 μm. (**B**) Violin plots displaying PIEZO2 and PGR immunofluorescence intensity using DH-Scores (digital histoscores). Individual data points are displayed for Ctrl and RIF endometrial samples ($n = 8$ per group, two-tailed Mann-Whitney test). (**C**) Pearson correlation analysis between PIEZO2 and PGR DH-Scores across all patient endometrial samples. PIEZO2 and PGR expression levels showed a significant positive correlation ($r = 0.6235$, $P = 0.0115$, two-tailed nonparametric Spearman correlation), consistent with a functional link between the two proteins. Blue dots, Ctrl; pink dots, RIF. (**D**) Quantitative RT-PCR analysis of *PIEZO2* and *PGR* expression in T-HESCs. Control cells (PIEZO2-Ctrl) and T-HESCs treated with PIEZO2 siRNA (PIEZO2-KD) were cultured on COL-I coated plates or uncoated plates (Vehicle) for 48h prior to RNA extraction. Expression was normalized to *GAPDH* ($n = 3$ per group, two-way ANOVA with Tukey's post hoc test). (**E**) Western blot analysis evaluating p-CaMKII (Thr286), p-FAK (Tyr397), total FAK, p-YAP (Ser127), and total YAP in T-HESCs. PIEZO2-Ctrl and KD cells were cultured on COL-I, or without COL-1 (Vehicle), with or without Y15 (FAK inhibitor). Lysates were obtained at 48h post-treatment and expression was normalized to β-actin ($n = 3$ independent experiments, two-way ANOVA with Tukey's post hoc test), with graphical quantification shown in Extended data Fig. 7B. (**F**) Quantitative RT-PCR analysis of *PGR* expression in T-HESCs cultured on COL-I with or without Y15. PIEZO2-Ctrl and KD cells were cultured on COL-I, or without COL-1 (vehicle), with or without Y15 (FAK inhibitor). RNA was extract at 48h post-treatment and expression was normalized to *GAPDH* ($n = 3$ per group, two-way ANOVA with Tukey's post hoc test). (**G**) Quantitative RT-PCR analysis of *PGR* expression in T-HESCs cultured on COL-I with or without BAPTA-AM (Ca^{2+} chelator) or KN93 (CaMKII inhibitor). PIEZO2-Ctrl and KD cells were cultured with or without COL-I. RNA was extracted at 48h post-treatment and expression was normalized to *GAPDH* ($n = 3$ per group, two-way ANOVA with Tukey's post hoc test). (**H**) Quantitative RT-PCR analysis of *PGR* expression in T-HESCs treated with TDI (LATS1/2 inhibitor) alone or in conjunction with verteporfin (VP, YAP-TEAD inhibitor). Ctrl and KD cells were cultured with or without COL-I. RNA was extracted at 48h post-treatment and expression was normalized to *GAPDH* ($n = 3$ per group, two-way ANOVA with Tukey's post hoc test). (**I**) Quantitative RT-PCR analysis examining decidualization markers (*IGFBP1*, *FOXO1*, *PRL*) in T-HESCs. PIEZO2-Ctrl and KD cells

were cultured as non-decidualized cells (Vehicle), decidualized (Dec) cells, or Dec cells with a vector overexpressing PGR-A (PRA+Dec) or PGR-B (PRB+Dec). After 48 h, RNA was extracted and expression was normalized to *GAPDH* ($n = 3$ per group, two-way ANOVA with Tukey's post hoc test). (**J**) Schematic model illustrating the PIEZO2-mediated uterine mechanosensing pathway. Under maternal stress, uterine hypercontraction generates mechanical forces that activate endometrial PIEZO2, triggering Ca^{2+}-dependent signaling that promotes collagen-rich ECM remodeling via IGF1-dependent paracrine communication. The PIEZO2-collagen axis activates FAK-Hippo-YAP signaling, driving nuclear YAP translocation and TEAD-dependent *Pgr* transcription. This mechanotranscriptional cascade reinforces progesterone responsiveness and prevents estrogen dominance, thereby safeguarding embryo implantation under stress conditions. In the absence of PIEZO2, this protective pathway is disrupted, leading to impaired PGR expression, defective decidualization, and implantation failure. Quantitative data are presented as mean ± SEM. ns, $P > 0.05$; *$P < 0.05$; **$P < 0.01$; ***$P < 0.001$.

Supplementary Files

This is a list of supplementary files associated with this preprint. Click to download.

- SupplementaryInformation20260911merge.pdf
- SupplementaryMaterials20261018merge.pdf
- nrreportingsummary.pdf
- UncroppedGelsandBlots20261020.pdf